Fiducial Reference Measurements for Satellite Ocean Colour Phase-2

Above-water field radiometry and data handling for ocean colour applications

FRM4SOC2-D6C

Title	Above-water field radiometry and data handling for ocean colour applications
Document reference	FRM4SOC2-D6C
Project	EUMETSAT – FRM4SOC Phase-2
Contract	EUMETSAT Contract No. EUM/CO/21/460002539/JIG
Deliverable	D6C (Above-water field radiometry and data handling)
Version	V.2.0
Date issued	20.08.2025

Prepared By	Approved by
Name: Giuseppe Zibordi	Name:
Organisation: EOScience	Organisation: EUMETSAT
Position:	Position:
Date: 20.08.2025	Date:
Signature:	Signature:

Document Control Table

Title	Above-water field radiometry and data handling for ocean colour applications
Document reference	FRM4SOC2-D6C
Project	EUMETSAT – FRM4SOC Phase-2
Contract	EUMETSAT Contract No. EUM/CO/21/460002539/JIG
Deliverable	D6C (Above-water field radiometry and data handling)
Version	V.2.0
Date Issued	20.08.2025

Document Change Record

Index	Issue	Revision	Date	Brief description	Issued by
1	1	0	01/09/2023	Original version	G. Zibordi
2	1	1	01/10/2023	Updated after EUMESAT revision	G. Zibordi
3	1	2	20/10/2023	Update after Consortium meeting	G. Zibordi
4	1	3	26/02/2024	Update with recent literature	G.Zibordi
5	1	4	25/07/2024	Revised accounting for ERB comments	G.Zibordi
6	1	5	20/03/2025	Updated with new sections	G.Zibordi
7	2	0	20/08/2025	Consolidated	G.Zibordi

Distribution List

Public at https://frm4soc2.eumetsat.int

Acronyms and Abbreviations

Acronym	Description
AAOT	Acqua Alta Oceanographic Tower
AERONET-OC	Ocean Color component of the Aerosol Robotic Network
CDOM	Colored Dissolved Organic Matter
CPL	Casablanca Platform
EUMETSAT	European Organisation for the Exploitation of Meteorological Satellites
FWHM	Full Width at Half Maximum
GDLT	Gustaf Dalen Lighthouse
GLR	Gloria Platform
GLT	Galata Platform
GSFC	Goddard Space Flight Center
GUM	Guide to the Expression of Uncertainty in Measurement
HLT	Helsinki Lighthouse
ILT	Irbe Lighthouse
IOCCG	International Ocean Colour Coordinating Group
IOP	Inherent Optical Properties
JRC	Joint Research Centre
OCI	Ocean Colour Instrument
OLCI	Ocean and Land Colour Instrument
QA	Quality Assurance
QC	Quality Control
ST7	Station 7
UTC	Coordinated Universal Time

Contents

1 Scope

The current document constitutes the deliverable D-6C (Above-water field radiometry and data handling for ocean colour applications) as required by the terms of the Invitation to Tender (ITT) No. 20/220036 "Copernicus – Fiducial Reference Measurements for Satellite Ocean Colour (FRM4SOC phase-2) issued by EUMETSAT.

The PMP is the controlling document that sets the principles for defining, organising, monitoring and controlling all activities within the project, including the identification and mitigation of possible risks.

2 Compatibility

Table 2-1. Compatibility

No.	Requirement		
1.	Guidelines on ensuring quality in field measurements and data handling methods		

3 Abstract

This document reviews the basic elements underpinning above-water radiometry and aims at providing guidance to scientists approaching *in situ* measurements for ocean colour applications targeting the assessment of satellite data products. The document, which benefits from extracts from various publications, complements the information already included in community protocols with a practical view to field equipment, instruments calibration and characterization, measurement practices, quality assurance, data reduction and processing, quality control, quantification of uncertainties and the application of *in situ* data to the assessment of satellite data products.

4 Introduction

Satellite data products satisfy application needs and ensure return on investment when they meet users' requirements. Therefore, the verification of user's requirements is a mandatory step for satellite data products, which are often generated through complex processes involving remote technology, indirect sensor calibration and, a number of algorithms and models. This verification process implies the assessment of satellite derived data products. Such a practice commonly requires access to *in situ* reference data of high accuracy, which entails: state-of-the-art absolute radiometric calibration and comprehensive characterization of field radiometers; accurate implementation of measurement protocols; execution of extensive *in-situ* and laboratory measurements and finally the processing of collected data applying severe quality control procedures.

Recognizing that '*Good (practically useful) data do not collect themselves. Neither do they magically appear on one's desk, ready for analysis and lending insight into how to improve processes*' (Vardemann *and* Jobe 2016), field radiometry has become an integral component of any satellite ocean colour mission. Indeed, *in situ* optical radiometry data are essential for: *i.* the indirect calibration (*i.e.*, system vicarious calibration) of satellite ocean colour sensors; *ii*. the assessment of satellite primary radiometric products such as the normalized water leaving radiance or the equivalent remote sensing reflectance; and finally *iii*. the development of bio-optical algorithms linking primary radiometric quantities to derived ocean colour data products such as water inherent optical properties or the concentration of optically significant water constituents.

Ocean colour *in situ* radiometry can benefit of various measurement methodologies: *in-water radiometry* relying on optical sensors operated in the water column; *above-water radiometry* relying on sensors looking at the sea by applying strict observation geometries; and finally *near-surface radiometry* with sensors operated just above or just below the surface. These methodologies, which were matter of extensive investigations and inter-comparisons, exhibit advantages and drawbacks. In-water radiometry allows for comprehensive characterizations of the water column, but implies relatively complex deployment operations and exhibits limitations in shallow or highly absorbing waters. Above-water radiometry, restricted to the determination of the sole water-leaving radiance or equivalent radiometric quantities, allows automated field operations, but measurement accuracy is affected by low sun zenith angles and moderate to high sea state. Near-surface methods allow for a relatively easy determination of the radiance leaving the water, but they are very sensitive to wave perturbations, which restrict their operation to a low sea state.

In the course of the last three decades a number of theoretical and applied investigations increasingly consolidated the physical basis underpinning the principles supporting ocean colour *in situ* radiometry. This led to the definition of various measurements protocols, even though still calling for advances allowing to lessen uncertainties in data products.

This document provides a series of recommendations on above-water radiometry to scientists approaching *in situ* measurements for ocean colour applications with focus on the assessment of satellite data products (see the schematic in Fig. 1). The document, that benefits from extracts from various publications, complements those information already included in community protocols with a practical view to field equipment, instruments absolute radiometric calibration and characterization, measurement protocols, quality assurance, data reduction and processing, quality control, quantification of uncertainties, application of data to the assessment of satellite data products.

5 On above-water radiometry

Radiometry is the science dealing with the properties of the electromagnetic radiation. In the specific case of ocean colour, it focusses on spectral radiance and plane irradiance in the visible and near-infrared regions of the spectrum.

Spectral radiance is a measure of the flux per unit solid angle, unit projected area and wavelength. This is a directional quantity commonly measured in $W\ m^{-2}\ nm^{-1}\ sr^{-1}$ through a conical field-of-view. Assuming a full-angle field-of-view θ, the related solid angle is $\Omega = 2\pi\cdot(1-\cos(\theta / 2))$. A basic assumption underlying radiance measurements is the spatial homogeneity of the flux in the sensor full-angle field-of-view. The most common ocean colour radiance quantity is the spectral water-leaving radiance $L_w(\lambda)$, which is the radiance emerging from below the water surface, quantified just above the surface and carrying information on the absorption and scattering properties of the optically significant water constituents as a function of wavelength λ.

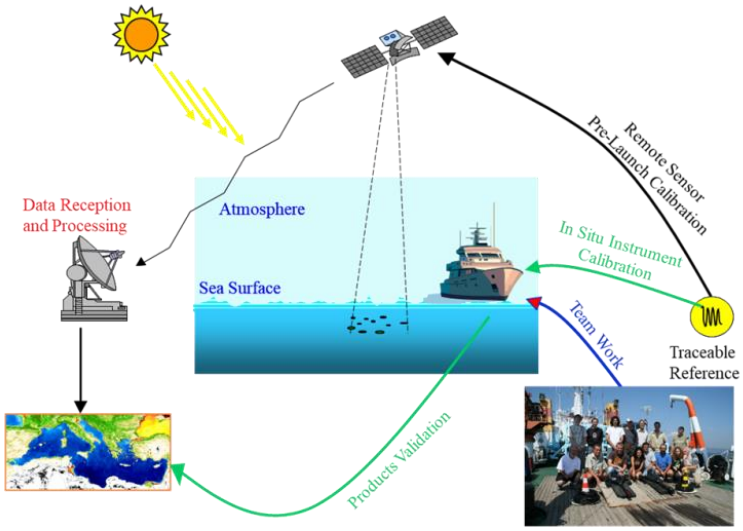

Figure 1. Schematic illustrating the assessment of satellite ocean colour data products centred on *in situ* reference measurements. Essential components of such a process are the field instruments, their absolute radiometric calibration and characterization, and an unavoidable number of contributions embracing, but not restricted to, the development and assessment of measurement methods and collaborative efforts on field activities and data handling, processing and archiving (adapted from Zibordi *et al.* 2020).

Spectral plane irradiance is a measure of the flux per unit surface area and wavelength. This quantity, commonly expressed in $W\ m^{-2}\ nm^{-1}$, is measured through a horizontal collector exhibiting cosine (angular) response. The accuracy of the cosine response and its stability over time, are fundamental elements of any plane irradiance sensor. Irradiance collectors are specifically designed for in-air or alternatively for in-water applications. A plane irradiance of relevance for above-water radiometry is the downward spectral irradiance $E_s(\lambda)$ quantified at the water surface.

The general above-water method considered here relies on the application of calibrated radiometers allowing for absolute spectral measurements of the total radiance from the water surface $L_T(\theta, \phi, \lambda)$ (which includes contributions from the water-leaving radiance and, additionally from sky- and sun-glint) and of the sky radiance $L_i(\theta', \phi, \lambda)$, performed with observation geometries defined by the relative azimuth angle ϕ between sensor and sun, and the viewing angle θ' specular to θ (*i.e.*, θ' =180–θ). The downward irradiance $E_s(\lambda)$ is the radiometric quantity allowing for the minimization of changes in illumination conditions that may affect $L_T(\theta, \phi, \lambda)$ and $L_i(\theta', \phi, \lambda)$ during measurement sequences. The remote sensing reflectance defined by $R_{rs}(\lambda) = L_w(\lambda)/E_s(\lambda)$ expressed in units of sr^{-1}, is one of the derived quantities of relevance for ocean colour investigations (for details see IOCCG 2019).

Measurements of $E_s(\lambda)$ should be performed simultaneously to $L_T(\theta, \phi, \lambda)$ and $L_i(\theta', \phi, \lambda)$. However, in the specific case of clear sky conditions essential for the validation of satellite data products, $E_s(\lambda)$ could be computed using actual atmospheric optical parameters such as the aerosol optical depth $\tau_a(\lambda)$. Nevertheless, this theoretical value is only relevant for the computation of $R_{rs}(\lambda)$ and it cannot support the minimization of possible illumination changes in $L_T(\theta, \phi, \lambda)$ and $L_i(\theta', \phi, \lambda)$ during the measurement sequence. The use of theoretical values of $E_s(\lambda)$, if computed using the same models applied for the determination of satellite radiometric data products (*e.g.,* by using the atmospheric diffuse transmittance $t_d(\lambda)$ as shown in Zibordi *et al.* 2009), increases the consistency between satellite and *in situ* data: this naturally assists the assessment of data products by reducing a source of uncertainty (*i.e.,* it removes uncertainty contributions due to the measured $E_s(\lambda)$ because the related uncertainties cancel out during the validation process).

It is also mentioned that when benefitting of a relative stability of the sky-radiance distribution during clear sky conditions, simultaneous measurements of $L_i(\theta',\phi,\lambda)$ and $L_T(\theta,\phi,\lambda)$ are not strictly necessary.

The water-leaving radiance $L_w(\theta, \theta_0, \phi, \lambda)$ with θ_0 indicating the sun zenith angle and (θ,ϕ) the viewing geometry, is determined by the following idealized measurement equation

$$L_w\ (\theta, \theta_0, \phi, \lambda) = L_T(\theta, \phi, \lambda) - \rho(\theta, \phi, \theta_0, W, \tau_a) L_i(\theta', \phi, \lambda) \quad (1)$$

where $\rho(\theta,\phi,\theta_0,W,\tau_a)$ is the sea surface reflectance factor (so-called ρ-factor) with the wind speed W conveniently expressing the sea state and the aerosol optical depth τ_a indicating dependence on the atmospheric optical properties

Equation (1) assumes that the sky-radiance L_i measured from a given direction and the modelled ρ-factor can satisfactorily allow for removing any sun- and sky-glint contributions in L_T. This naturally implies that the assumptions supporting the theoretical determination of the ρ-factor closely apply for the actual measurement conditions. For example, ρ-factors determined for clear sky conditions are unlikely to represent observations heavily affected by cloudiness.

Additionally, the sun- and sky-radiance contributions reflected by the sea surface into the field-of-view of the L_T sensor are from a number of directions depending on the orientation of the facets created by waves. Because of this, sky-radiance and wave-slope distributions not accurately representing the actual measurement conditions may lead to an increase of uncertainties with θ_0 and W, which are key parameters for the theoretical determination of the ρ-factors. Consequently, a fundamental aspect of above-water radiometry is the selection of the measurement geometry. The suitable ones should allow for minimizing the variability of glint perturbations in L_T measurements and thus maximize the probability that the modelled ρ-factors accurately account for the sun- and sky-radiance contributions reflected by wave facets into the sensor field-of-view..

Mobley (1999) suggested a viewing angle θ of 40° and a relative azimuth ϕ of 135° as the most appropriate to minimize sun glint perturbations in above-water radiometry. This recommendation is fully supported by the lower and more stable values of modelled ρ-factors determined for diverse sun zeniths and sea states with ϕ =135° (see Fig. 2). However, this ideal geometry applied to actual field measurements may lead to appreciable perturbations by the superstructure of deployment platforms, with impact increasing with sun zenith. In fact when using ϕ = 135°, the L_T radiometer would generally look at the sea close to the deployment structure or at its shadow. Because of this, the selection of the relative azimuth angle needs to trade-off between a measurement geometry minimizing glint effects and that minimizing infrastructure perturbations: ϕ = 90° is considered a viable solution (see Fig.s 2 and 3).

Finally, considering the relevant impact of wave perturbations, the determination of $L_w(\theta,\phi,\lambda)$ should rely on successive measurements sequences lasting a few minutes each. These are essential to support quality control procedures targeting tests on the stability of $E_s(\lambda)$ and $L_i(\theta,\phi,\lambda)$, and more importantly of $L_T(\theta,\phi,\lambda)$. Details on these tests are provided in the section *On quality control.*

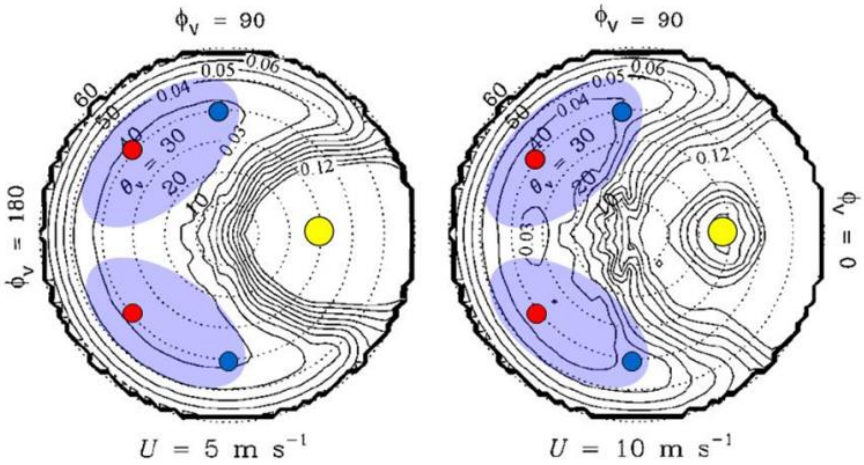

Figure 2. Distributions of ρ-factors as a function of the viewing and relative azimuth angles for wind speeds of 5 and 10 $m\ s^{-1}$, and sun zenith of 30° (adapted from Mobley 1999). The yellow filled circle mirrors the sun position. The shadowed light-blue areas highlight viewing geometries most suitable for above-water radiometry. The blue and red filled circles indicate the L_T viewing geometries relying on ϕ = 135° and ϕ = 90°, respectively.

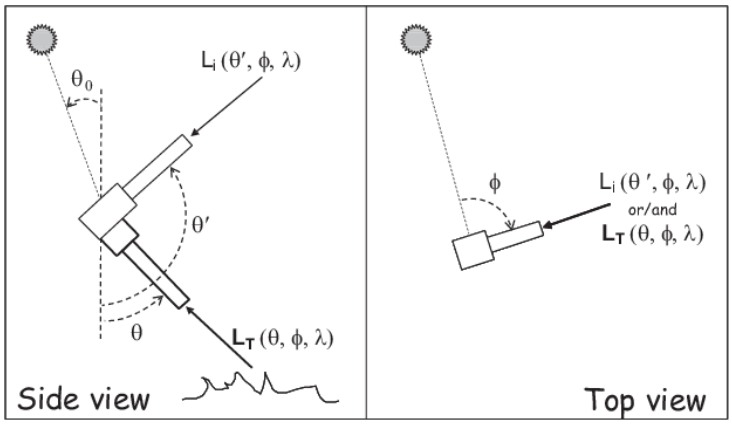

Figure 3. Measurement geometry commonly applied for above-water radiometry: relative azimuth ϕ = 90° and viewing angle θ = 40° implying θ' = 180° – θ, with θ_0 indicating the sun zenith angle (reprinted from IOCCG 2019).

For completeness it is mentioned that above-water methods relying on relative measurements of the radiance from the sea and of the total downward irradiance reflected by a horizontal, homogeneous and lambertian plaque (*e.g.*, see Carder *and* Steward 1985), are often considered an alternative to the application of calibrated radiance and irradiance sensors allowing independent measurements of $E_s(\lambda)$, $L_i(\theta,\phi,\lambda)$ and $L_T(\theta,\phi,\lambda)$. However, this method is challenged by the difficulty of ensuring reliable field implementations (*i.e.*, minimizing perturbations by close obstacles, and enforcing accurate geometries and proper handling of the plaque), which would affect the accuracy of measurements and the quantification of their uncertainties.

Further, a number of processing solutions were proposed as alternatives to Eq. (1). All these solutions attempt an optimization of the sky-glint removal, that is the minimization of any residual sky radiance affecting $L_w(\lambda)$ (see Lee *et al.* 1997, Gould *et al.* 2000, Ruddick *et al.* 2006, Simis and Olsson 2013, Kutser *et al.* 2013, Groetsch *et al.* 2017). However, their effectiveness in reducing data collected during clear sky conditions is not definitively proven (Pitarch *et al.* 2020). Because of this, considering the primary objective of supporting the application of *in situ* radiometric measurements for the validation of satellite ocean colour data products naturally related to clear sky conditions, it is suggested to strictly rely on the basic measurement equation given by Eq. (1) .

Finally, a relevant element, often overlooked in above-water radiometry, is the need to correct $L_w(\theta,\theta_0,\phi,\lambda)$ for the non-nadir view of the L_T sensor. This correction implies assumptions on the bidirectional reflectance properties of the water and the application of consistent modelling solutions (see section *On data reduction and processing*). This need should discourage the adoption of diverse values of ϕ for operational measurements performed with different sun elevations. In fact, correction factors determined for diverse measurement geometries would be very likely affected by different uncertainties, which are difficult to quantify and which would naturally lead to potential intra-measurement inconsistencies.

6 On ρ-factors

Simulated ρ-factors are commonly determined by dividing theoretical values of the total radiance L_T in the direction (θ,ϕ) by the sky-radiance L_i from the direction (θ,ϕ'), ideally accounting for the field-of-view of the L_T and L_i sensors. As already anticipated, the accuracy of computed ρ-factors is constrained by the ability to exactly determine $L_T(\theta,\phi,\lambda)$ through the modelling of sea surface reflectance features and consequently the sun- and sky-light contributions reflected into the field-of-view of the L_T sensor. It is mentioned that the involved processes develop over *i*. time scales largely determined by the sensors sampling times and *ii*. spatial scales varying from a few up to several tens of cm^2 as a function of the sensor field-of-view and of the sensor height above the sea surface.

Valuable and extensively applied ρ-factors are those proposed by Mobley (1999). These were determined from simulations performed at λ = 550 nm by modelling: *i.* the sea surface perturbations as a function of wind speed through the Cox-Munk parameterizations of wave slopes; and *ii*. the sky-radiance distribution accounting for aerosols and multiple scattering, but neglecting polarization effects. Alternative ρ-factors were successively proposed by Mobley (2015), also determined at λ = 550 nm, but modelling: *i*. the sea surface perturbations accounting for wave height and slope variance; and *ii*. the sky-radiance distribution by accounting for polarization effects, but neglecting aerosols and multiple scattering. In summary, while the early ρ-factors from 1999 do not account for polarization, the latter ρ-factors from 2015 determined for a purely molecular sky are expected to represent extreme polarization effects because of the absence of any depolarization contribution by the aerosols.

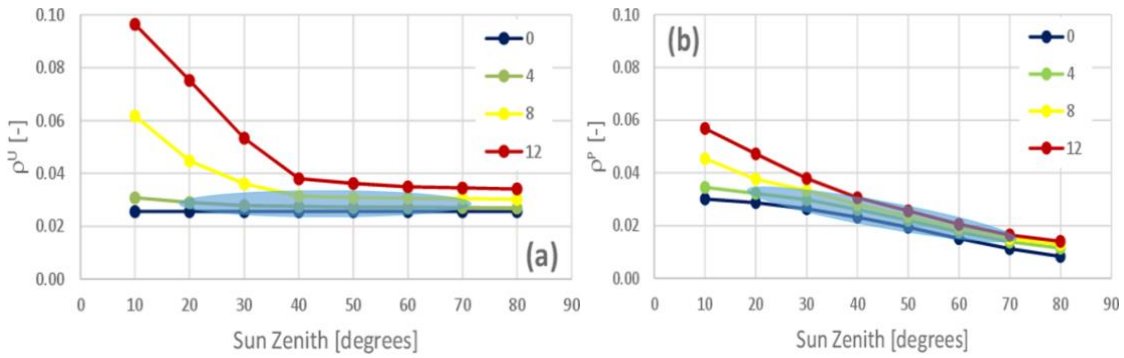

Figure 4. Value of the ρ-factors for θ = 40° and ϕ = 90°, determined neglecting polarization effects (ρ^U) in the left panel and accounting for them (ρ^P) in the right panel (adapted from Zibordi 2015). The shaded areas highlight the values of ρ^U and ρ^P leading to the determination of close $L_w(\theta,\theta_0,\phi,\lambda)$.

The ρ-factors proposed by Mobley in 1999 and those in 2015, exhibit differences more marked for low and high sun zenith angles (see Fig. 4). An experimental assessment (Zibordi 2016) indicated slightly better performance of the ρ-factors determined neglecting the polarization effects, when restricting their evaluation to measurements performed with relatively low wind speed (tentatively W<5 ms^{-1}) and away from low and high sun zenith angles (tentatively 20° < θ_0 < 70°). This finding suggests a confident application of the ρ-factors from Mobley (1999), at least until new spectral ρ-factors accounting for aerosol type and load, and ideally polarization effects (*e.g.,* Harmel 2023), are comprehensively assessed.

7 On optical radiometers and their fore-optics

When evaluating above-water radiometers for field operations, it is important to appreciate that diverse applications may have different requirements and that diverse technologies may have reached a different stage of maturity. Because of this, any specific application should be sustained with instruments able to satisfy requirements, duly accounting for the direct or indirect support obtainable from the community to ideally minimize individual efforts on instruments absolute radiometric calibration and characterization, and also on data processing.

Optical radiometers can be separated into two major classes: multispectral and hyperspectral.

Multispectral radiometers have a few spectral bands typically 10 *nm* wide commonly chosen to match those of satellite sensors. The individual spectral bands are realized through spectral band-pass filters coupled to photodetectors. A potential weakness of this technology, aside the limited number of spectral bands, is the spectral response outside the nominal band-passes (the so-called out-of-band response), which may become the source of measurement errors varying with the spectral shape of the incoming light. Significant advantage offered by multispectral radiometers is their relatively simple and robust optics design, which normally minimizes sensitivity to polarization and stray light (light from one region of the spectrum interfering with light from another region due to scattering or reflections in the optical system), and consequently lessen the need for instrument characterizations.

Hyperspectral radiometers exhibit a number of spectral bands typically varying from tens to hundreds. These radiometers use dispersive optical elements (*i.e.,* diffraction gratings or prisms) allowing to realize spectral bands continuously distributed across the spectrum with widths commonly comprised between 3 and 10 *nm*. Opposite to multi-spectral radiometers, the higher complexity of the optics due to various reflecting and diffracting components, make hyperspectral radiometers more affected by stray lights and sensitive to polarization and temperature with effects varying with wavelength. When evaluating the performance of hyperspectral radiometers (*e.g.*, see Table 1), it is important to distinguish between *spectral sampling* defining the distance between the centre-wavelengths of contiguous bands, and *spectral resolution* defining the amplitude of each band (see Fig. 5).

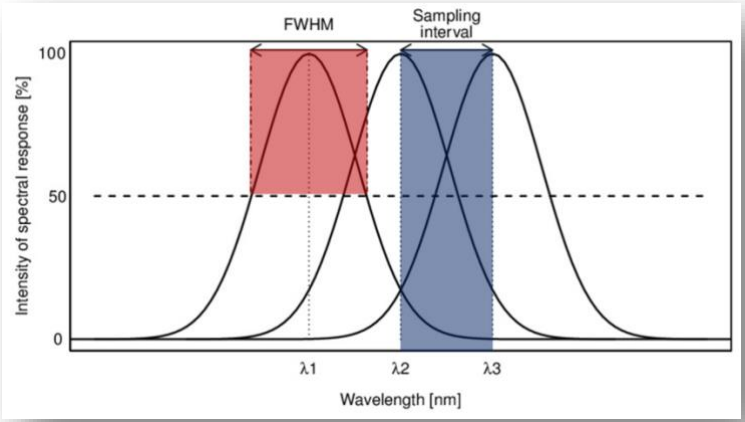

Figure 5. Spectral resolution determined by the full-width-half-maximum (FWHM) of the spectral bands and spectral sampling (*i.e.,* sampling interval) determined by the distance between spectral bands (adapted from Zemek 2014).

In summary, multispectral radiometers largely compensate the limitation of sampling at a few discrete spectral bands, still matching those of most satellite ocean colour sensors, with less demanding instrument characterizations. Conversely, hyperspectral instruments, which offer the major advantage of a continuous distribution of spectral bands across the visible and near-infrared portions of the spectrum, imply a larger number of characterizations. Definitively, some of these characterizations may be applicable to classes of instruments with a major community benefit.

Table 1. Recommended specifications for hyperspectral radiometers of relevance for satellite ocean colour validation activities (after IOCCG 2019).

Spectral Range:	380 to 900 nm (an extension in the ultraviolet is desirable)
Spectral Resolution:	3-10 nm (FWHM)
Spectral Sampling:	1-3 nm (or at least 2 times the spectral resolution)
Wavelength Accuracy:	10 % FWHM resolution
Wavelength Stability:	5 % FWHM of resolution
Signal-to-Noise Ratio:	1000:1 (at minimum)
Stray Light Rejection:	10^{-5} (of the maximum radiometric signal at each spectral band)
FOV Maximum (full-angle):	5° (for above-water)
Temperature Stability:	Specified for 0–45°C
Linearity:	Correctable to 0.1 %

The field-of-view is a relevant parameter in above-water radiometry. In fact, due to the high variability of sun- and sky-glint contributions to $L_T(\theta,\phi,\lambda)$, large field-of-views would increase the averaging of wave effects while small field-of-views would imply a higher variability across successive measurements. It is recognized that restricting the determination of $L_i(\theta,\phi,\lambda)$ to any full-angle field-of-view lower than 20° would only have marginal impact on the quantification of $L_w(\theta,\phi,\lambda)$. Nevertheless, a general recommendation would be to use full-angle field-of-views not appreciably exceeding 5°. Some investigation showed the major advantage of a full-angle field-of-view of approximately 1°, which allows for an efficient flagging of those measurements affected by high variance due to glint perturbations (Zibordi 2012).

The angular response of irradiance collectors is unlikely to exhibit ideal cosine dependence. Ultimately, the cosine error (*i.e.*, the deviation from the ideal cosine response) may largely vary from sensor to sensor of the same series (see also *On the absolute radiometric calibration and characterization of field radiometers*). Consequently, it is essential that the non-cosine response of any individual irradiance sensor is always characterized and that cosine errors do not exceed the thresholds recommended in protocols (see IOCCG 2019).

Finally, the application of multispectral radiometers using filter-wheel technologies should not be considered for above-water radiometry due to the consequent asynchronous collection of the spectral data required for the determination of $L_i(\theta,\phi,\lambda)$ and $L_T(\theta,\phi,\lambda)$. However, a strict quality control of measurements was shown to minimize the impact of such a major drawback (Zibordi *et al.* 2021).

8 On the absolute radiometric calibration and characterization of field radiometers

The sentence '… *adequately sampled, carefully calibrated, quality controlled, and archived data for key elements of the climate system will be useful indefinitely'* (Wunsch *et al.* 2013), clearly conveys the message that relevant data will be permanently valuable if: adequately sampled, implying that appropriate measurement strategies were adopted and implemented; carefully calibrated, implying that the necessary absolute radiometric calibrations and characterizations were performed for the measuring instruments; quality controlled, implying that state of the art processing and quality control were applied; and finally archived, implying the existence of solutions allowing the community to access the data. It is emphasized that calibration, leading to the conversion of sensors output from relative to physical units, is a fundamental element in the above list of general requirements.

Metrological traceability indicates a common origin of the reference, for instance the international reference systems, ensuring that measurements are comparable regardless of instrument, time, location and operator. Metrological traceability is thus *the sequence of measurement standards and calibrations that are used to relate a measurement result to a reference*. In the case of optical radiometers, traceability implies their absolute radiometric calibration through a radiance or irradiance source, commonly based on a 1000 W quartz-halogen FEL lamp with tungsten coiled filament, directly or indirectly calibrated with respect to the freezing temperature of gold. Consequently, *absolute radiometric calibration* can be defined as the practice consenting to compare the output from an instrument with that of a calibration standard (commonly called working standard) with known uncertainty determined through the traceability pyramid (see Fig. 6). This process encompasses the determination of the absolute radiometric response (*i.e.*, responsivity) of the sensor and leads to establishing the relationship providing measurements with defined units and uncertainties from the output of the instrument.

Characterization, complementary to absolute radiometric calibration, is the determination of the distinctive features of an instrument allowing to account for deviations from its expected ideal performance. These may include: temperature dependence; response change with time; polarization sensitivity; stray light effects; and deviations from the ideal angular response for irradiance sensors (see Table 2).

In the following sections, the generic term calibration will identify the combined application of both absolute radiometric calibration and instrument characterizations.

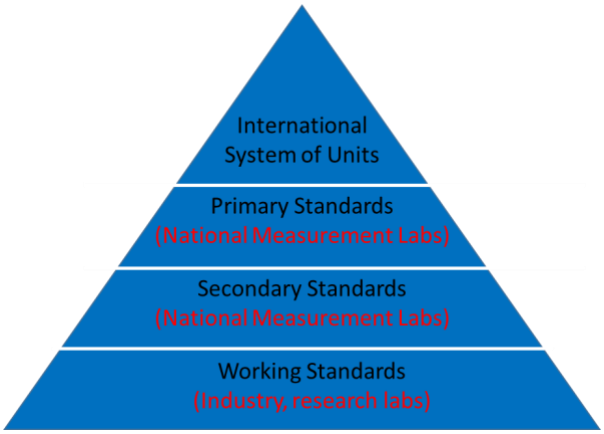

Figure 6. Traceability pyramid illustrating the *unbroken chain of comparisons* supporting absolute radiometric calibrations. Uncertainties increase from the apex to the base during each comparison process leading to the creation of the *working standards* commonly applied in calibration laboratories.

Following Zibordi *et al.* (2019) the conversion from relative to physical units of the radiometric quantity $\Im(\lambda)$ (either irradiance $E(\lambda)$ or radiance $L(\lambda)$) at wavelength λ is performed through

$$\Im(\lambda) = C_{\Im}(\lambda)\, \aleph(\lambda)\, DN(\Im(\lambda)) \quad (2)$$

where $C_{\Im}(\lambda)$ is the in-air absolute radiometric calibration coefficient (determining the responsivity) and $\aleph(\lambda)$ (for simplicity only expressed as a function of λ) a correction factor accounting for all deviations from the ideal performance of the measuring instrument. Specifically, in the case of an ideal radiometer $\aleph(\lambda)=1$, but more in general

$$\aleph(\lambda)= \aleph_i(i(\lambda))\, \aleph_j(j(\lambda)) \ldots \aleph_k(k(\lambda)) \quad (3)$$

where $\aleph_i(i(\lambda))$, $\aleph_j(j(\lambda))$, …, and $\aleph_k(k(\lambda))$ are the correction terms, assumed independent for the different contributions indexed by i, j, …, k affecting the non-ideal performance of the considered radiometer. It is specified that the term $DN(\Im(\lambda))$ indicates the digital output corrected for the dark value (*i.e.,* the actual digital output $DN(\Im(\lambda))$ from which the dark value $D0(\lambda)$ measured by obstructing the entrance optics, has been subtracted).

Absolute radiometric calibrations and characterizations require facilities providing access to laboratory standards of spectral irradiance, reflectance plaques, spectral filters, regulated power supplies. Unsurprisingly, the majority of scientists carrying out field measurements do not have easy access to these facilities. Still, the necessary support may come from manufacturers or reference laboratories sustained by major measurement programs. Standardization of instruments obtained by adopting a restricted number of instrument models targeting applications would definitively make the characterization process more focused and consequently effective for the community. It is emphasized that inter-calibrations among laboratories are essential to identify issues in absolute calibration and characterization set-ups, radiometric sources, or even protocol implementations. An example of laboratory inter-comparison for absolute radiometric calibrations of a radiance sensor is shown in Fig. 7. This example, aside from quantifying differences through ratios of calibration factors from diverse laboratories, shows uncertainties determined for each compared value and additionally assumes that one of the calibration laboratories (*i.e.*, the National Institute of Standards and Technology) can provide reference data.

For detailed information on radiometers absolute calibrations and characterizations, the reader is addressed to the *Protocols on Field Radiometry for Ocean Colour Validation* (IOCCG 2019) and to *Guidelines for individual OCR full characterisation and calibration* (Vabson *et al.* 2023). Examples of characterizations specific for hyperspectral radiometers widely used by the community are provided in Fig.s 8-11.

Table 2. Absolute calibration and characterizations expected for optical radiometers together with their envisaged temporal occurrence (reprinted from IOCCG 2019). This table was built on the assumption that the characterizations, the related uncertainties and the expected target uncertainties for data products obtained from specific radiometers or systems, allow for ideally considering a number of class based characterizations. Definitively, strict target uncertainty requirements, or instrument series exhibiting large differences in radiometer-to-radiometer performance, may suggest the need for individual characterization of each radiometer. It is emphasized that occasional, initial and class-based characterizations should be taken over by major measurement programs in collaboration with manufacturers and established reference laboratories.

	Regular	Occasional	Initial	Class-based
Radiometric responsivity	X			
Spectral response		X		
Out-of-band & stray-light		X		
Immersion factor (irradiance)			X	
Immersion factor (radiance)				X
Angular response			X	
Linearity				X
Integration time				X
Temperature response				X
Polarization sensitivity				X
Dark signal	X			
Temporal response				X
Pressure effects				X

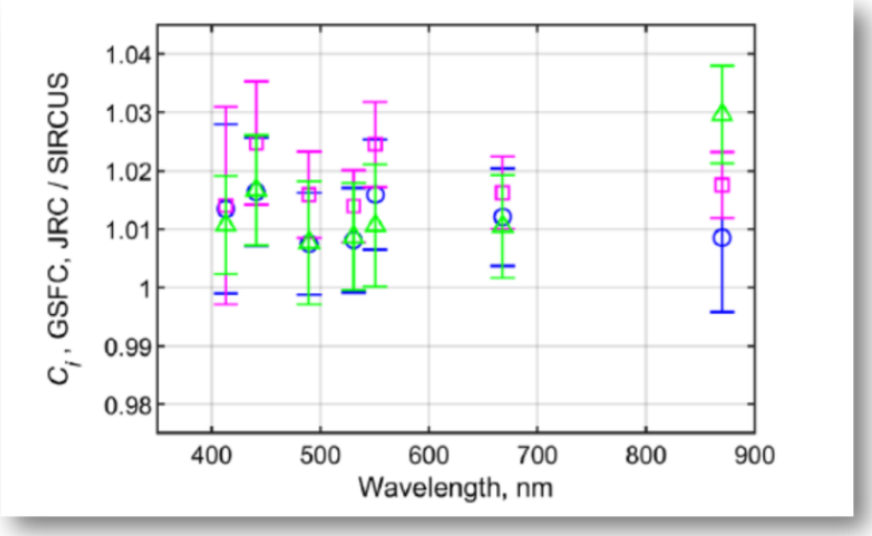

Figure 7. Ratio of absolute calibration coefficients determined for a multispectral radiance sensor at the Goddard Space Flight Center of the National Aeronautics and Space Administration (GSFC, open circles and squares) using an integrating sphere and those determined at the Marine Optical Laboratory of the Joint Research Centre (JRC, triangles) using an FEL lamp in combination with a reflectance plaque, over those determined by the National Institute of Standards and Technology (NIST) obtained through laser-based facility for Spectral Irradiance and Radiance Responsivity Calibrations using Uniform Sources (SIRCUS) (reprinted from Johnson *et al.* 2022).

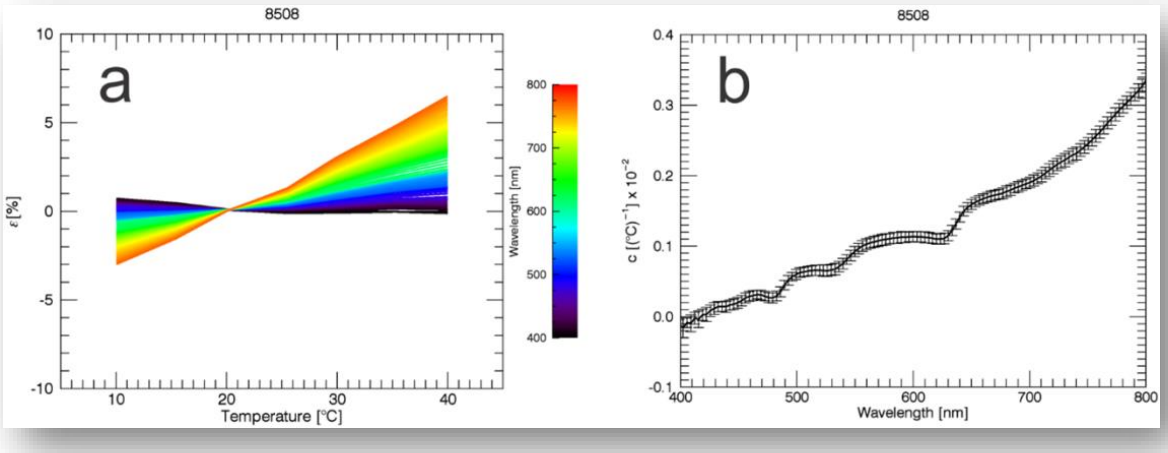

Figure 8. Relative change in spectral response ε as a function of temperature determined with respect to the reference response at temperature T=20° *C* (*panel a*), and temperature coefficient c(λ) in units of $(°C)^{-1}$ (*panel b*) for the hyperspectral radiometer SAM-8508 (reprinted from Zibordi *et al.* 2017). It is essential to appreciate that an accurate determination of changes in response with temperature requires information on the actual working temperature of the optical sensor. Because of this, when radiometers do not have internal temperature sensors, there is the need to conceive and apply solutions allowing to quantify correction factors for temperature response (see *On quality assurance*).

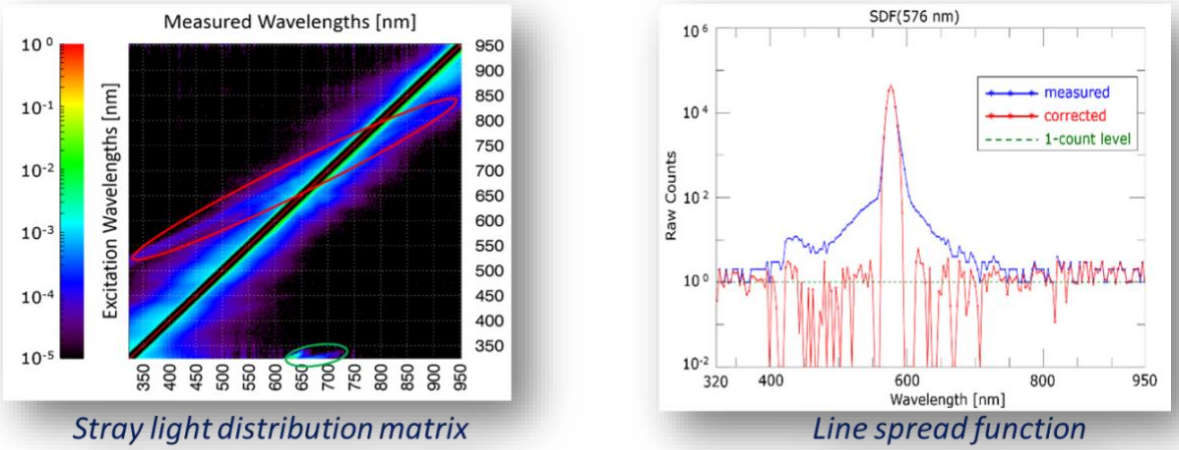

Figure 9. Stray light distribution matrix (*left panel*) for the hyperspectral radiometer SAM-8346 and application of the stray light correction matrix to a monochromatic signal at 576 *nm* (*right panel*). In the left panel the measurement and excitation wavelengths are on the x and y axes in units of *nm*, respectively. The values of the matrix coefficients, in normalized (raw) counts, are displayed in log-scale. The green and red ellipses highlight spectrally extended stray light perturbations. The black straight lines near the diagonal identify the in-band response regions. In the right panel the measured and the corrected signals are shown in blue and red, respectively. The 1-*count* level is indicated by the dashed line (reprinted from Talone *et al.* 2016). It is likely that instrument batches manufactured applying the same design and optical components, exhibit very similar stray light perturbations. Once verified, this would allow to confidently apply the same stray light correction procedure to all the radiometers from the batch.

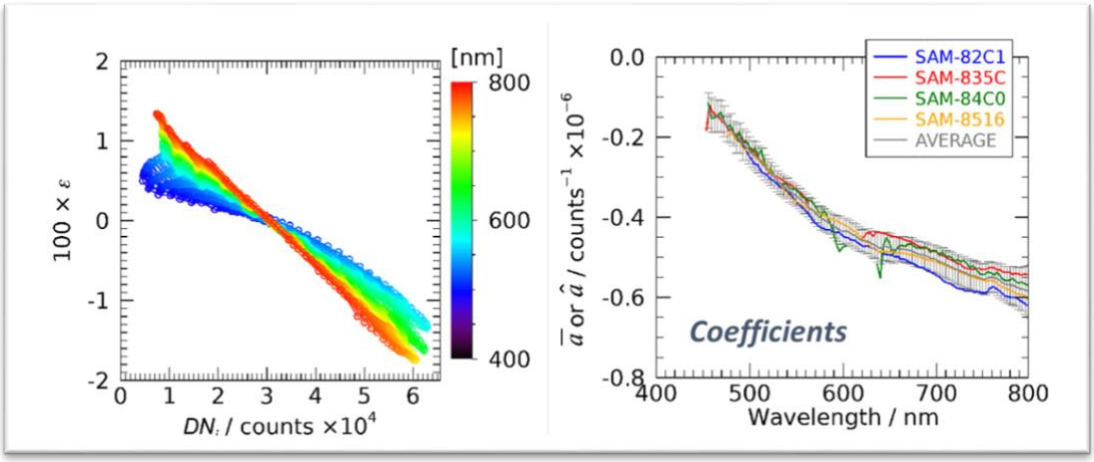

Figure 10. Relative spectral non-linearity factors ε in percent, determined for SAM-8516 as a function of the output counts normalized at 3×10^4 *counts* (left panel) and non-linearity factors $\bar{a}$ in $counts^{-1} \times 10^{-6}$ (right panel) as well as the corresponding average value $\hat{a}$ with the related standard deviations, for the hyperspectral radiometers SAM-82C1, SAM-835C, SAM-84C0, and SAM-8516 (reprinted from Talone *and* Zibordi 2018). As for stray light perturbations, instrument batches manufactured applying the same design and optical components may exhibit very similar non-liner response. In this case too, once verified, the same non-linear correction procedure could be applied to each radiometer from the same batch.

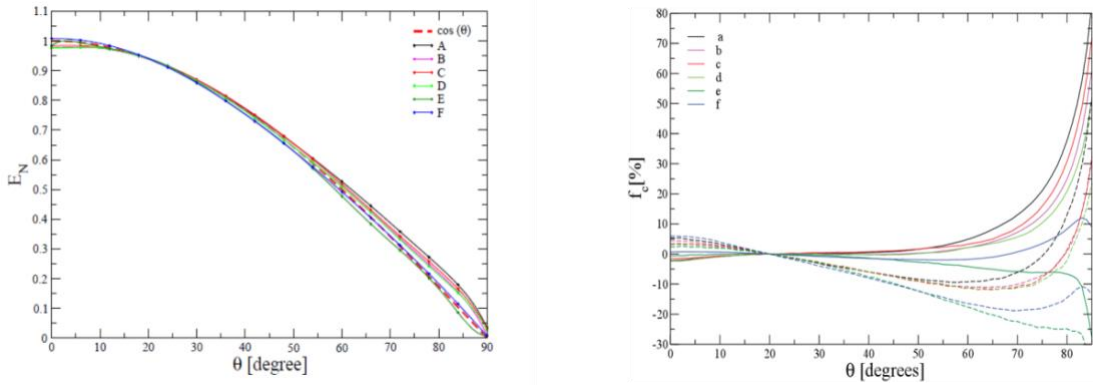

Figure 11. In-air cosine spectrally averaged responses E_N normalized at 20° (left panel) for various hyperspectral radiometers with respect to the ideal cosine response and, spectrally averaged in-air and in-water values of the cosine error $f_c(\theta) = E_N(\theta)/\cos(\theta) - 1$ in percent (right panel) displayed using continuous and dashed lines, respectively (reprinted from Mekoui *and* Zibordi 2014). Opposite to other non-ideal instrument performances, the non-cosine response generally largely varies across individual collectors. This implies the need for individual characterizations for each irradiance sensor.

9 On ancillary data and metadata

In addition to radiometric measurements performed strictly following protocols and supported by the related calibration coefficients and characterization factors, the processing of above-water data requires a number of additional information likely handled through an effective data management system. Relevant ancillary data and metadata include: date and time (expressed in *UTC*); longitude and latitude; bottom depth, cloud cover and sea state; wind speed and direction (even though of limited use, barometric pressure and, air and water temperature, should be also considered). Further, if data are collected from non-fixed deployment platforms such as ships, it is fundamental that roll, pitch and heading of the platform are recorded during each measurement sequence to determine the fulfilment of measurement requirements on viewing geometry and platform stability. In particular, tilt determined from the composition of roll and pitch values, might influence measurement accuracy of $E_s(\lambda)$ and, to a lesser extent, of $L_i(\theta',\phi,\lambda)$ and $L_T(\theta,\phi,\lambda)$. In fact any significant sensor tilt would affect the basic assumption of plane irradiance for $E_s(\lambda)$ measurement requiring the sensor is operated horizontally.

Similarly, in the case of $L_i(\theta,\phi,\lambda)$ and $L_T(\theta,\phi,\lambda)$, any large tilt would lead to measurements not fulfilling pre-defined observation and illumination geometries (see the section *On quality control*). Important, for systems exhibiting a variable acquisition rate (*i.e.,* adjusting the integration time as a function of light intensity with integration times that may exceed hundreds of milliseconds), roll and pitch must be over sampled with respect to the radiometric measurements to allow for an effective screening of data.

Finally, in view of supporting the implementation of future processing schemes relying on advanced spectral ρ-factors, the aerosol optical properties including at least the spectral optical depth should be measured and duly archived. It is mentioned that measurements of the aerosol optical depth are already needed for the computation of theoretical $E_s(\lambda)$ when not actually measured (*e.g.,* see Zibordi *et al.* 2009). Last, while performing actual $E_s(\lambda)$ measurements, the estimate of its diffuse $E_i(\lambda)$ and direct $E_D(\lambda)$ components through a rotating-shadow band as displayed in Fig. 12 (see also Zibordi *et al.* 2002 and Hooker *et al.* 2003) is important for the determination of corrections minimizing of the effects of the non-cosine response of irradiance sensors (see *On data reduction and processing*).

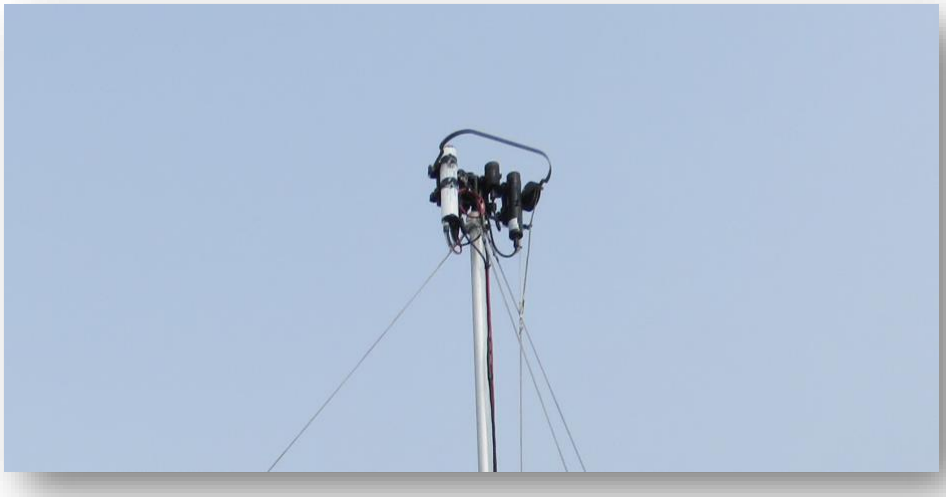

Figure 12. Set of E_s sensors deployed on a pneumatic mast equipped with a rotating shadow band attachment. The band, while moving above the sensors, obstructs the direct sun irradiance $E_D(\lambda)$ and allows for an estimate of the diffuse component $E_i(\lambda)$ of the total downward irradiance $E_s(\lambda)$.

10 On quality assurance

Quality assurance (QA) entails processes-oriented actions leading to the correct execution of measurements. Consequently, quality assurance practices imply ensuring pre-deployment calibration to any component of the measurement systems and putting efforts into proper installing and operating the equipment, correctly implementing measurement protocols, and in general taking any action leading to the execution of measurements free from operational mistakes and only marginally affected by environmental perturbations (*e.g.*, wave and cloud perturbations, changes in illumination conditions and optical properties of water while performing a measurement sequence).

The superstructure of deployment platforms are often the source of shading and reflection in field measurements performed in their proximity: these perturbations, which are often difficult to quantify, need to be minimized in view of avoiding significant measurement errors. Superstructure perturbations affecting $E_s(\lambda)$ measurements can be avoided by deploying the E_s radiometers above any structure element that may be seen in the field-of-view of the irradiance sensor and also well away from sources of pollution. Still, it is recalled that radiometers need daily maintenance (*e.g.,* inspection and cleaning). Telescopic poles operated at convenient locations of superstructures generally offer a practical solution to such a need.

Equally relevant, but often overlooked is the location of L_i and L_T radiometers whose measurements must also be performed from a position that minimizes the impact of shading, reflection and water surface perturbation by the superstructure. On ships, ideally profiting of a pole allowing to deploy L_i and L_T radiometers at some height, a favourable measurement location is offered by the bow. Assuming a suitable measurement geometry obtained with the sun azimuth normal to the port or starboard sides, the L_T radiometer should look at portions of the sea undisturbed by ship wakes. Still allowing for some flexibility in the measurement geometry, it is essential that the heading direction of the ship allows for the L_T radiometer to view the sea surface at a distance d at least larger than the superstructure height h (Hooker *and* Morel 2003,

Hooker *and* Zibordi 2005). This requirement often implies restricting the data collection to within specific azimuth limits with respect to the ship heading. In the case of fixed deployment structures, whose heading cannot be changed, measurements ideally not affected by superstructure perturbations are only possible during certain hours of the days. This implies choosing a deployment location for the L_i and L_T radiometers allowing to perform measurements unaffected by superstructure perturbations at the most convenient time for the validation of satellite data products (*i.e.,* tentatively around local noon).

Superstructure perturbations affecting above-water radiometric data products may naturally exhibit a spectral dependence with effects more pronounced in the red and near-infrared. Specifically, the work of Talone *and* Zibordi (2019) showed superstructure perturbations well within 1% in the visible spectral region and exceeding 2% in the near infrared for $R_{rs}(\lambda)$ determined with $\phi = 90°$ and $d \approx h$ when relying on a deployment platform characterized by *low-reflectance*. However, for equivalent measurement conditions but considering the same platform characterized by *high reflectance* (*i.e.,* a white colour superstructure), perturbations increased up to approximately 1% in the blue-green and well exceeded 2% in the red and near infrared spectral regions (see Fig. 13). This result, still qualitative and referred to a specific deployment structure, indicates the need for extreme care in determining the distance d from the structure for which the data can be ideally assumed free from major superstructure perturbations.

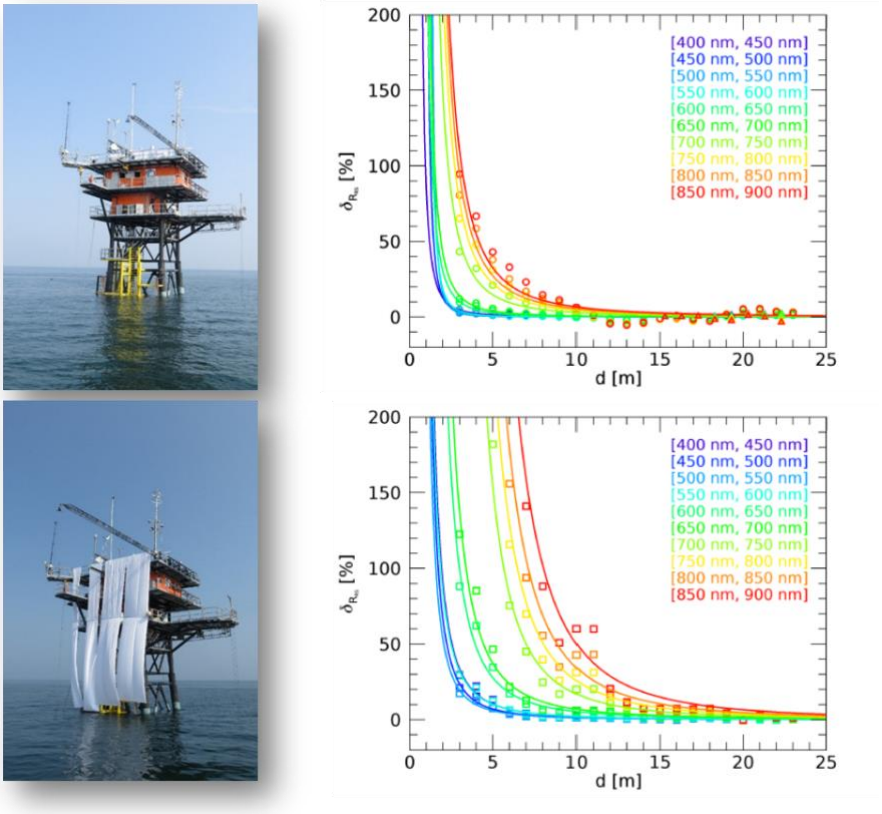

Figure 13. Spectral changes $\delta_{R_{RS}}(\lambda)$ affecting $R_{RS}(\lambda)$ as a function of the distance from the superstructure for actual measurement conditions (*i.e.*, *low reflectance*) in the upper panels and additionally, for measurement conditions worsened by the increased reflectance of the superstructure (*i.e.*, *high reflectance*) in the lower panels (after Talone *and* Zibordi 2019). The superstructure height h is 17 m. It is assumed that $\delta_{R_{RS}}(\lambda) = 0$ in the far field (*i.e.*, well away from the superstructure): this is tentatively fulfilled with d~17 m for the *low reflectance* case and with d ~ 25 m for the *high reflectance* case.

Field radiometric data may also require the minimization of potential bottom perturbations and adjacency effects in satellite data (Zibordi *et al.* 2009), both hindering the actual comparability between *in situ* and satellite data products. This suggests performing validation measurements at geographic locations free from bottom perturbations (which depend on bottom depth and type, and the optical properties of water) and adjacency effects (which largely depend on the distance from land, land cover, and the atmospheric and marine optical properties). While bottom perturbations could be roughly estimated by guessing a spectral diffuse attenuation coefficient $K_d(\lambda)$ and bottom reflectance (see Zibordi *et al.* 2002), a distance larger than tentatively 10 *km* appears a reasonable trade-off to minimize the impact of adjacency effects in satellite data (Bulgarelli *and* Zibordi 2018, Bulgarelli *and* Zibordi 2020).

11 On the radiometers response to temperature

Ambient temperature may largely affect the response of optical sensors. This is made evident by the dark signal, which suggests that any measurement sequence should at least include appropriate determinations of the sensor dark counts (*i.e.*, the output counts in the absence of any input flux). When sensors do not allow for an automatic determination of the dark signal (*e.g.*, in the absence of an internal shutter), dedicated measurements should be performed by occulting the sensor fore-optics. An inappropriate quantification of the dark signal would lead to poor bias corrections of $L_i(\theta',\phi,\lambda)$, $L_T(\theta,\phi,\lambda)$ and $E_s(\lambda)$ measurements with the unavoidable introduction of measurement errors in $L_w(\theta,\phi,\lambda)$. Still, corrections for temperature response should be applied accounting for sensors characterizations when the derived quantity is likely to be affected. This step requires access to the internal temperature of the sensor or alternatively to the ambient temperature, depending how the characterization was performed.

Ambient temperatures representative of the radiometer working one (*i.e.*, the temperature at which the radiometer is in thermal equilibrium) cannot be assumed equal to the air temperature. In fact the direct sun-light hitting the radiometer would definitively impact its working temperature, which may vary across radiometers of the same system. A practical solution allowing to reliably support the correction for the temperature response is achievable by increasing the thermal capacity of the radiometer using an external sleeve made of material having the same thermal conductivity of the radiometer case, and then considering as ambient temperature that measured inside the sleeve in the proximity of the radiometer case (see Fig. 14). This approach showed differences between the ambient temperature measured inside the sleeve and the actual air one varying from negligible to slightly higher than +5°C when the radiometer was exposed to the direct sun light during clear sky with air temperatures not exceeding 27°C.

Figure 14. RAMSES sensor equipped with an external steel sleeve allowing to measure the ambient temperature in the proximity of the sensor case (left side), paralleled to the regular sensor (right side).

The above solution, however, requires some engineering effort and regular temperature measurements inside the sensor sleeve. An alternative solution is offered by the possibility to quantify the sensor working temperature directly from the dark signal.

When considering a specific radiometer series (*e.g.*, RAMSES by TriOS, Germany) not benefitting of an internal thermistor, darks are obtained by the output of elements of the detector array painted black, or from the whole detector elements once obstructing the entrance aperture with a cap.

Laboratory investigations of the dark signal from RAMSES radiometers show a clear dependence with temperature. However, the sensitivity of the dark signal on temperature increases with the integration time (see left panel in Fig. 15). This suggests that most accurate information on darks could be obtained with the highest integration time. Figure 15 (right panel) illustrates such a dependence of the dark values determined with diverse integration times. Remarkable, the temperature dependence on dark counts displayed in the left panel of Fig. 15, documents a low sensitivity below tentatively 30 °C. This anticipates extremely low accuracy for radiometers working temperatures determined using the dark signal at a low ambient temperature.

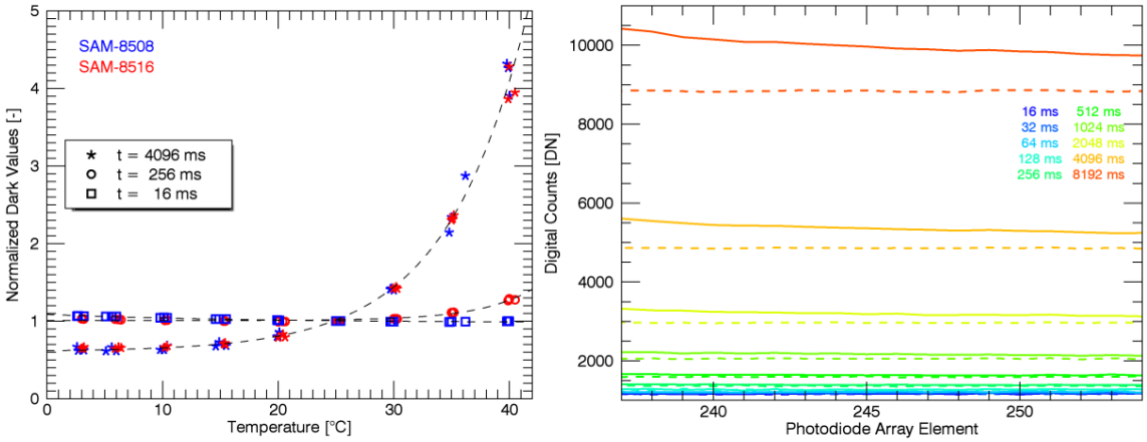

Figure 15. Dark signal values normalized at T=25 °C (left panel) determined for RAMSES SAM-8508 and RAMSES SAM-8516 with different integration times t, and counts (right panel) determined from the occulted elements of SAM-8516 with the entrance optics closed (dashed lined) and alternatively illuminated by an integrating sphere with saturation occurring for t > 256 ms (after Zibordi et al. 2017).

Figure 15 (right panel) also shows that the charge overflow (*i.e.*, the transfer of charge from saturated elements of the array to the nearby ones), prevents determining the darks from the dark-painted elements simply applying a high integration time without obstructing the entrance aperture. In fact, the black-painted cells would be affected by the charge overflow from the nearby elements affected by saturation due to over exposition to a light source.

Figure 16 (left panel) shows the relationship between ambient temperature T and dark counts DN as obtained from laboratory characterizations from four RAMSES radiometers through the fitting equation

$$T = -T_C + S * \ln(DN - DN_C) \quad (4)$$

where the digital dark value DN_C, the temperature T_C and the slope factor S are obtained from the fit.

The standard deviation $\sigma_T(DN)$ of the averaged values, which largely increases with a decrease of the dark counts, determines the uncertainties of the fitting function. In particular, whereas an uncertainty in the working temperature T expressed by $\sigma_T(DN)$ is approximately 2°C with 1×10^4 counts, its value approaches 5°C with 3×10^3 counts.

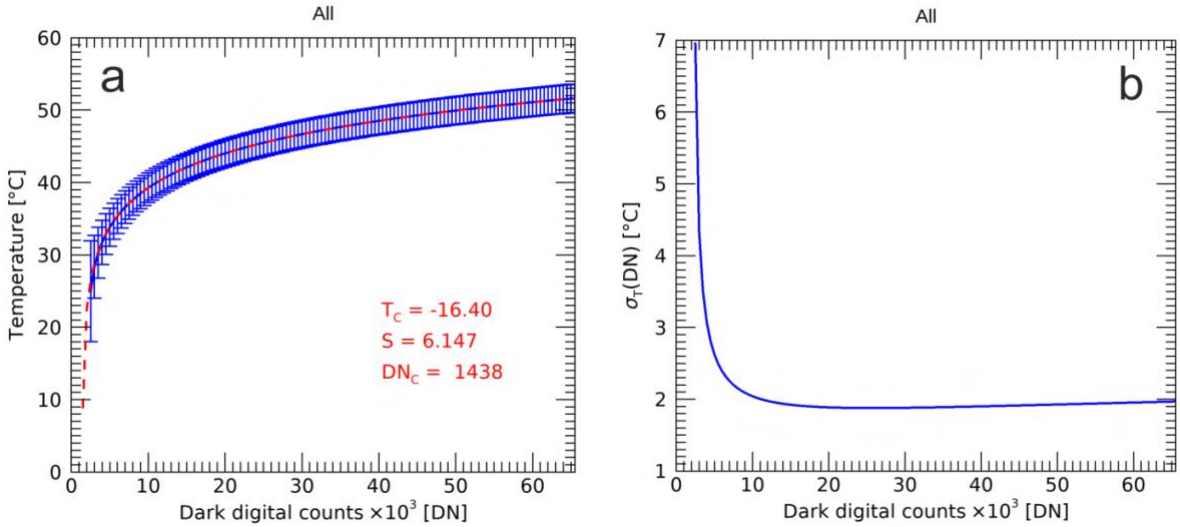

Fig. 16. Working temperature T (left panel) and related standard deviation $\sigma_T(DN)$ (right panel) as a function of the dark counts DN determined from the characterization of four RAMSES radiometers. The error bars in the left panel indicate ±1 $\sigma_T(DN)$ (Talone and Zibordi, submitted).

A comprehensive analysis of the uncertainties affecting the determination of the working temperature from the dark signal, as well the alternative use of the air temperature instead of the ambient temperature perceived by the radiometer, are presented in Zibordi and Talone (2025). The analysis performed applying solutions assumed valid for the class of instruments based on dark counts obtained occluding the entrance optics of the radiometers and applying an integration time t = 4096 ms, indicate the possibility to perform temperature corrections with uncertainty lower than 1% in the 400-800 nm interval for working temperatures T higher than approximately 30°C. Uncertainties may already exceed 3% at 800 nm for T lower than approximately 30°C due to the lesser sensitivity of temperature retrievals with the decrease of dark counts.

Still recognizing that the ambient temperature T would exhibit differences with the air temperature T_a, Zibordi and Talone (2025) show the possibility to apply operational temperature corrections with uncertainties lower than 1% in the 400-800 nm spectral interval when setting $T = T_a + (\delta T/2)$ with values of $T - T_a$ uniformly distributed and the max difference δT between T and T_a not exceeding +10°C. This alternative approach may complement, or even replace, that relying on ambient temperatures determined from the dark counts of RAMSES radiometers, which is only viable for T > 30°C.

12 On data reduction and processing

Above-water measurement sequences, ideally performed during clear sky conditions, should comprise:

i. a number N_T of sea-radiance measurements for determining $L_T(\theta,\phi,\lambda)$;
ii. a number N_i of sky-radiance measurements for determining $L_i(\theta',\phi,\lambda)$; and
iii. measurements of the downward irradiance $E_s(\lambda)$ simultaneous to the N_T sea-radiance and N_i sky-radiance ones.

N_i and N_T do not need to be identical when assuming stability of the sky radiance during the execution of each sequence. Still, a relatively large number of N_T measurements (*i.e.*, tentatively a few tens) is important to statistically address the impact of wave perturbations.

Raw data are converted to physical units accounting for the absolute radiometric calibration coefficients and any additional characterization factor. Substantial differences in successive absolute radiometric calibration coefficients, such as those determined before and after deployments lasting more than a few weeks, must be carefully evaluated. Justified and significant differences, tentatively exceeding 1-2%, should lead to their interpolation as a function of time.

For each measurement sequence performed during ideal illumination conditions, $L_i(\theta',\phi,\lambda)$ can be determined by the average of the N_i sky-radiance data. Conversely, $L_T(\theta,\phi,\lambda)$ should be subject to quality control tests aiming at minimizing measurement perturbations. These are separately addressed in the section "*On quality control*".

The normalized water-leaving radiance $L_{WN}(\lambda)$, which is the radiance that would occur with nadir view, no atmosphere, the sun at the zenith and at the mean sun-earth distance, is given by

$$L_{WN}(\lambda) = L_W(\theta,\phi,\lambda)\; C_Q(\theta,\phi,\theta_0,\lambda,\tau_a,IOP,W)\; C_A(\theta_0,t_d\,,D) \tag{5}$$

where the correction factor $C_Q(\theta,\phi,\theta_0,\lambda,\tau_a,IOP,W)$ minimizes the impact of bidirectional effects due to the non-nadir view of the L_T radiometer (including that of the water-air transmittance) and of the illumination conditions, with τ_a and *IOP* indicating the aerosol optical depth and the inherent optical properties of water, respectively. The factor C_A indicates the ratio $E_0(\lambda)/E_s(\lambda)$ where $E_s(\lambda)$ is here taken as the average value of the downward irradiance during each measurement sequence. It is mentioned that if actual measurements of $E_s(\lambda)$ are not available, C_A can be computed as $(D^2 t_d(\lambda)\cos\theta_0)^{-1}$ with D accounting for the sun-earth distance as a function of the day of the year and $t_d(\lambda)$ the atmospheric diffuse transmittance (Zibordi *et al.* 2004).

The most common approach applied for the minimization of bidirectional effects is that proposed by Morel *et al.* (2002) for Case-1 waters (*i.e.*, chlorophyll-*a* dominated), and hereafter called *Chla*-based. Field radiometry, however, encompasses measurements performed in optically complex waters for which the application the *Chla*-based approach may lead to large uncertainties. This suggests the application of schemes minimizing bidirectional effects in optically complex coastal waters. Among the various approaches proposed in literature, the one considered here is that by Lee *et al.* (2011). This correction, hereafter called *IOP*-based, provides the major advantage of relying on the retrieval of water *IOP*s from $L_W(\theta,\phi,\lambda)$ itself.

An experimental study focused on the comparison of the *Chla*- and *IOP*-based approaches, still restricted to the bidirectional effects due to non-nadir view, showed average relative differences between the two correction approaches varying between 10% and 40% in the blue and green spectral regions with standard deviation of 10–25% (Talone *et al.* 2018). By using *in situ* reference data to quantify the uncertainties affecting the correction factors from the two approaches for waters exhibiting diverse optical complexities, the study indicated relative spectrally and water dependent uncertainties varying between 20% and 60% for the *Chla*-based approach, with the highest values affecting the blue and red regions. Conversely, the *IOP*-based approach showed relative uncertainties within 20–35% and lower dependence on wavelength and water type.

The implementation of the *Chla*-based approach benefits of lookup tables to compute corrections, still restricted to key ocean colour centre-wavelengths 412, 443, 490, 510, 560, 620 and 660 nm. Nevertheless, equivalent lookup tables were recently produced by the Observatoire Océanologique de Villefranche-sur-Mer applying the same processing solutions as in Morel *et al.* (2002), but with a spectral resolution of 5 nm and extending the spectral range to 350–700 nm (Bernard Gentili, unpublished), with the additional possibility of indexing the clear sky illumination conditions with values of τ_a = 0.05, 0.10, 0.2, 0.4 and 1.0.

A brief introduction to both the *Chla*- and *IOP*-based correction approaches is provided hereafter.

The *Chla*-based approach minimizes the dependence of $L_W(\theta,\phi,\lambda)$ on the viewing geometry and solar zenith following Eq. (6) with the factor $C_Q(\theta,\phi,\theta_0,\lambda,\tau_a,IOP,W)$ determined by

$$C_Q^{Chla}(\theta,\phi,\theta_0,\lambda,\tau_a,IOP,W) = \frac{\Re(0,W)}{\Re(\theta,W)}\frac{Q(\theta,\phi,\theta_0,\lambda,\tau_a,Chla)}{f(\theta_0,\lambda,\tau_a,Chla)}\frac{f(0,\lambda,\tau_a,Chla)}{Q(0,0,0,\lambda,\tau_a,Chla)} \quad (6)$$

where $\Re$ accounts for combined reflection/refraction effects on the downward irradiance and upwelling radiance propagating through the sea surface, Q is the Q-factor indicating the ratio of upward irradiance to upwelling radiance just below the surface, and f relates the irradiance reflectance to the water *IOP*s. While τ_a expresses the dependence on the atmospheric optical properties, the chlorophyll-*a* concentration *Chla* indicates the dependence on *IOP*s. The values of *Chla* can be estimated applying regional band-ratio algorithms (Zibordi *et al*. 2009b).

The *IOP*-based approach (Lee *et al.* 2011) relies on the application of the following equation relating $L_W(\theta,\phi,\lambda)$ to the inherent optical properties of water

$$\begin{aligned} L_W(\theta,\phi,\lambda) = {} & E_s(\lambda)\left(G_0^w(\theta,\phi,\theta_0)+G_1^w(\theta,\phi,\theta_0)\frac{b_{bw}(\lambda)}{a(\lambda)+b_b(\lambda)}\right)\frac{b_{bw}(\lambda)}{a(\lambda)+b_b(\lambda)} \\ & +\left(G_0^p(\theta,\phi,\theta_0)+G_1^p(\theta,\phi,\theta_0)\frac{b_{bp}(\lambda)}{a(\lambda)+b_b(\lambda)}\right)\frac{b_{bp}(\lambda)}{a(\lambda)+b_b(\lambda)} \end{aligned} \quad (7)$$

where, $E_s(\lambda)$ is the downward irradiance, $a(\lambda)$ is the water absorption coefficient (due to the contributions of pure sea-water $a_w(\lambda)$, detritus plus CDOM $a_{dg}(\lambda)$ and phytoplankton $a_{ph}(\lambda)$), $b_b(\lambda)$ is the water backscattering coefficient (given by the sum of the contributions of water molecules $b_{bw}(\lambda)$ and particles $b_{bp}(\lambda)$).

The *IOP*-based approach implies the determination of $a(\lambda)$ and $b_{bp}(\lambda)$ from Eq. (7) using the model coefficients $G_0^w(\theta,\phi,\theta_0)$, $G_1^w(\theta,\phi,\theta_0)$, $G_0^p(\theta,\phi,\theta_0)$ and $G_1^p(\theta,\phi,\theta_0)$ derived from simulated $L_W(\theta,\phi,\lambda)$. From the retrieved values of $a(\lambda)$ and $b_{bp}(\lambda)$, the normalized water-leaving radiance $L_{WN}(\lambda)$ is then determined using the model coefficients $G_0^w(0,0,0)$, $G_1^w(0,0,0)$, $G_0^p(0,0,0)$ and $G_1^p(0,0,0)$ using

$$\begin{aligned} L_{WN}(\lambda) = {} & E_0(\lambda)\left(G_0^w(0,0,0)+G_1^w(0,0,0)\frac{b_{bw}(\lambda)}{a(\lambda)+b_b(\lambda)}\right)\frac{b_{bw}(\lambda)}{a(\lambda)+b_b(\lambda)} \\ & +\left(G_0^p(0,0,0)+G_1^p(0,0,0)\frac{b_{bp}(\lambda)}{a(\lambda)+b_b(\lambda)}\right)\frac{b_{bp}(\lambda)}{a(\lambda)+b_b(\lambda)} \end{aligned} \quad (8)$$

where $E_0(\lambda)$ is the mean extra-atmospheric solar irradiance.

Independent investigations confirmed an expected better suitability of the *Chla*-approach for measurements performed in Case-1 waters, while the *IOP*-approach appears applicable to any water type (Gleason *et al.* 2012, Talone *et al.* 2018). For completeness it is mentioned that the above Eq.s (7) and (8) can be formulated to restrict corrections to the sole non-nadir view (see IOCCG 2019). This solution is convenient for a direct comparison of above- and in-water derived values of $L_W(\lambda)$ requiring that the viewing geometries are reconciled.

Definitively, the two approaches lead to corrections exhibiting significant differences. This is shown by the diverse range and values of the corrections displayed in Fig. 17 for $L_W(\theta,\phi,\lambda)$ for different water types: compare the values of the spectral corrections ε^{Chla} and ε^{IOP} determined for the same input $L_W(\theta,\phi,\lambda)$.

Finally, as already anticipated, $L_{WN}(\lambda)$ or the corresponding $R_{RS}(\lambda)$, are the fundamental radiometric quantities supporting satellite ocean colour applications. In fact, they carry information on the optically significant materials suspended or dissolved in the water, independent from the atmospheric perturbation and the viewing and illumination geometries. As an example of $L_{WN}(\lambda)$ spectra representative of diverse water types, Fig. 18 displays $L_{WN}(\lambda)$ spectra from diverse geographic regions characterized by diverse water types spanning from the ultra-oligotrophic waters of the Eastern Mediterranean Sea (EMED) to the highly absorbing waters of the Baltic Sea (BLTS), with a variety of intermediate optical complexities created by diverse concentrations of optically significant constituents (for details see Zibordi *and* Berthon 2024).

Aside corrections for the non-isotropic distribution of light in the water, it is important to consider the need for additional corrections minimizing the non-deal performance of radiometers (see IOCCG 2019). For convenience, simply restricting such corrections to the effects of cosine-errors in $E_s(\lambda)$ and assuming the irradiance collector is operated perfectly horizontal, an empirical correction scheme is provided in Zibordi *and* Bulgarelli (2007) and re-proposed in IOCCG (2019). Such a method requires knowledge of the diffuse $E_i(\lambda)$ and direct $E_D(\lambda)$ components of $E_s(\lambda)$, and obviously of the cosine-error affecting the specific irradiance sensor. Its application is expected to constrain below 1-2% the uncertainties in $E_s(\lambda)$ due to the cosine-error.

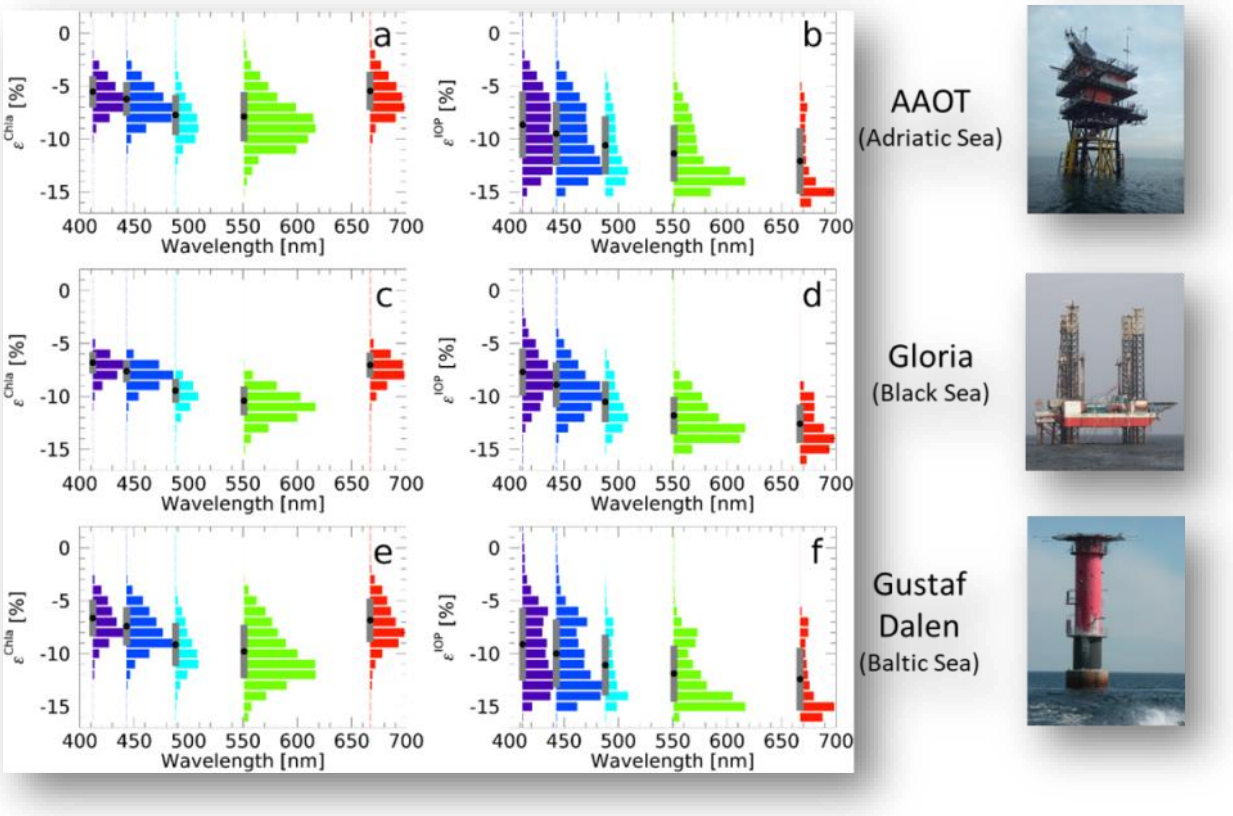

Figure 17. Percent corrections ε^{Chla} and ε^{IOP} applied to $L_W(\theta,\phi,\lambda)$ for the removal of the sole non-nadir viewing dependence through the *Chla*-based (left panels) and *IOP*-based (central panels) approaches, respectively. The $L_W(\theta,\phi,\lambda)$ data refer to sites (right panels) representative of waters exhibiting different optical complexity: the Acqua Alta Oceanographic Tower (AAOT) and the Gloria site for waters characterized by various concentrations of sediments and coloured dissolved organic matter; and the Gustaf Dalen site characterized by water exhibiting high concentrations of coloured dissolved organic matter (reprinted from Talone *et al.* 2018).

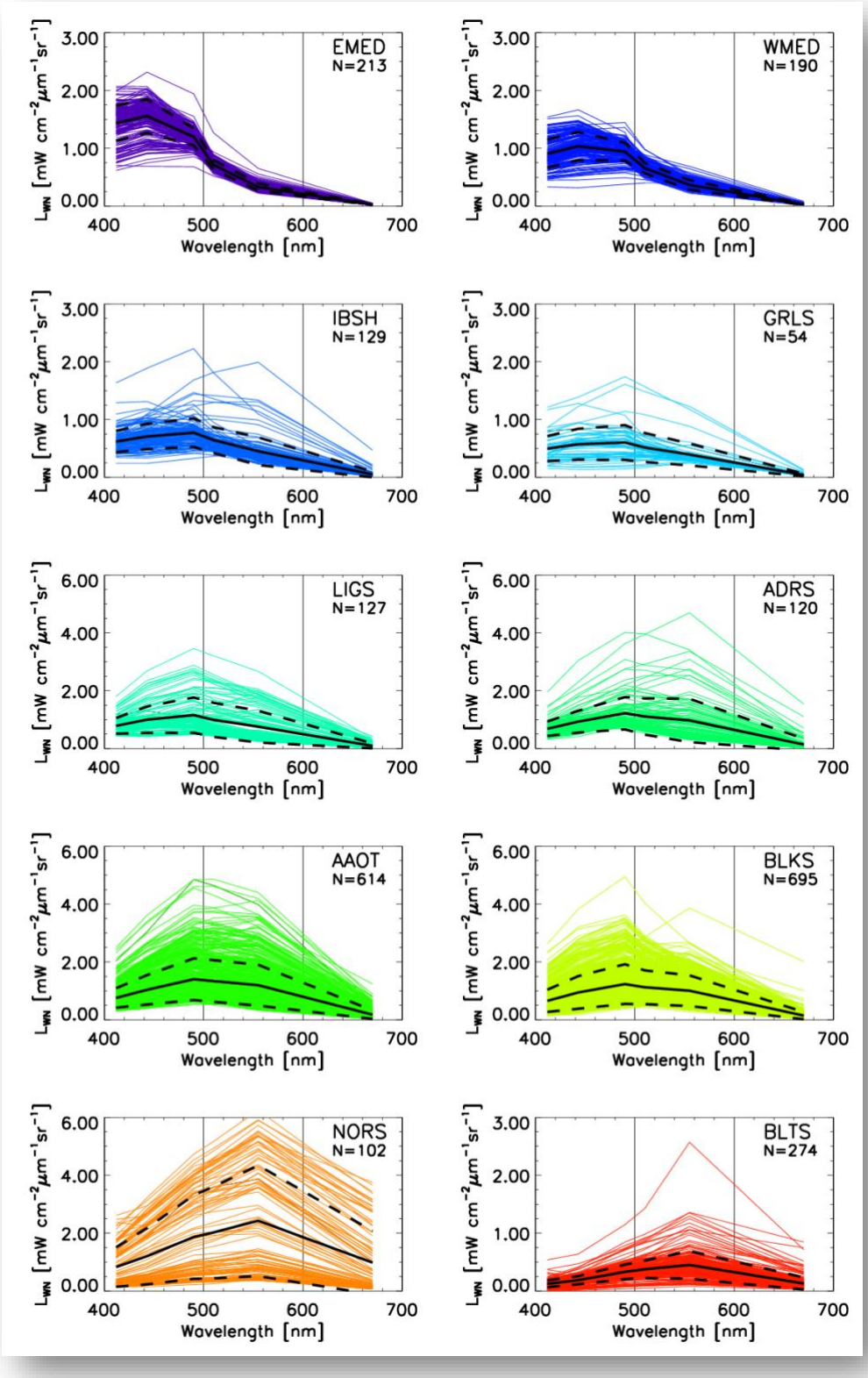

Figure 18. Spectra of $L_{WN}(\lambda)$ from different geographic regions characterized by diverse water types: Eastern Mediterranean Sea (EMED), Western Mediterranean Sea (WMED); Iberian Shelf (IBSH); Greenland Sea (GRLS); Ligurian Sea (LIGS); Adriatic Sea (ADRS); Acqua Alta Oceanographic Tower site (AAOT) in the northern Adriatic Sea; Black Sea (BLKS); North Sea (NORS); Baltic Sea (BLTS). N indicates the number of spectra displayed in the panel. The continuous black lines indicate mean values while the dashed lines indicate ± 1 standard deviation (after Zibordi *and* Berthon 2024).

13 On quality control

Quality control (QC) practices include all post-measurement actions supporting the provision of high-quality data. These entail any step aiming at flagging questionable data products. Clearly, automated procedures embedded in data processing are quite essential for the quality control of datasets resulting from a large number of field measurements such as time-series from a variety of sites or multiple oceanographic campaigns. Below are listed a number of tests to be considered for the quality control of above-water radiometric data.

A first QC test should exclude from successive processing all those measurement sequences not satisfying constrains on instrument performance, viewing geometry, environmental conditions and superstructure perturbations. This implies verifying that: the dark values of sensors are below a given threshold; tilts affecting L_T, L_i and E_s sensors do not exceed predefined thresholds (tentatively 5° for $L_T(\theta,\phi,\lambda)$ and $L_i(\theta',\phi,\lambda)$ measurements, and ideally 1-2° for $E_s(\lambda)$, still allowing larger values for this latter when the sun zenith angles are low); the values of ϕ_0 are within limits minimizing superstructure perturbations in $L_T(\theta,\phi,\lambda)$; the wind speed W does not exceed 15 $m\ s^{-1}$ (and more strictly 7 $m\ s^{-1}$) to allow for the application of meaningful ρ–factors.

The N_T sea-radiance and N_i sky-radiance measurements may exhibit high variability across individual measurement sequences, generally completed within a few minutes. A high variability of sea-radiance measurements is generally explained by relatively high sea state conditions, and additionally by low sun zenith angles and potential cloud perturbations. A high variability characterizing sky-radiance measurements is explained by cloudiness. Because of this, in view of minimizing the perturbing effects due to sun-glint or even foam contamination or clouds in $L_T(\theta,\phi,\lambda)$, and similarly exclude the potential for cloud perturbations in $L_i(\theta',\phi,\lambda)$, data pre-processing should include quality control tests to remove measurement sequences exhibiting standard deviations above a given threshold for the N_T and N_i measurements. In the specific case of the N_T sea-radiance measurements, standard deviation thresholds should be considered for the radiance values in at least one spectral band: the selection of a red or near-infrared band would definitively increase sensitivity to sun-glint perturbations. These spectral thresholds, as determined and applied to specific asynchronous multispectral measurements (see Zibordi *et al.* 2021), are typically constrained in the range of 0.1-0.2 $mW\ cm^{-2}\ \mu m^{-1}\ sr^{-1}$ for the sea-radiance measurements and in the range of 0.02-0.03 $mW\ cm^{-2}\ \mu m^{-1}\ sr^{-1}$ for the sky-radiance measurements, both referring to clear sky and low sea state.

The above filtering process commonly affects measurement sequences exhibiting high sun-glint perturbations: consequently it mostly impacts measurement sequences performed with low sun zeniths (tentatively with θ_0 lower than 20°) and mild-to-high wind speed (tentatively with W > 5 ms^{-1}). This implies that measurements sequences passing the former test are not largely affected by sun-glint. Nevertheless, they might still be perturbed by excessive sky-glint due to sky-radiance contribution from very bright regions of the sky reflected by the sea surface into the field-of-view of the L_T sensor. Then, for each measurement sequence, data affected by excessive sky-glint contributions could be removed by determining L_T as the average of a given percent of the N_T measurements exhibiting the lowest radiance values (tentatively between 10-20% of the data), opposite to the use of the average of all N_T measurements.

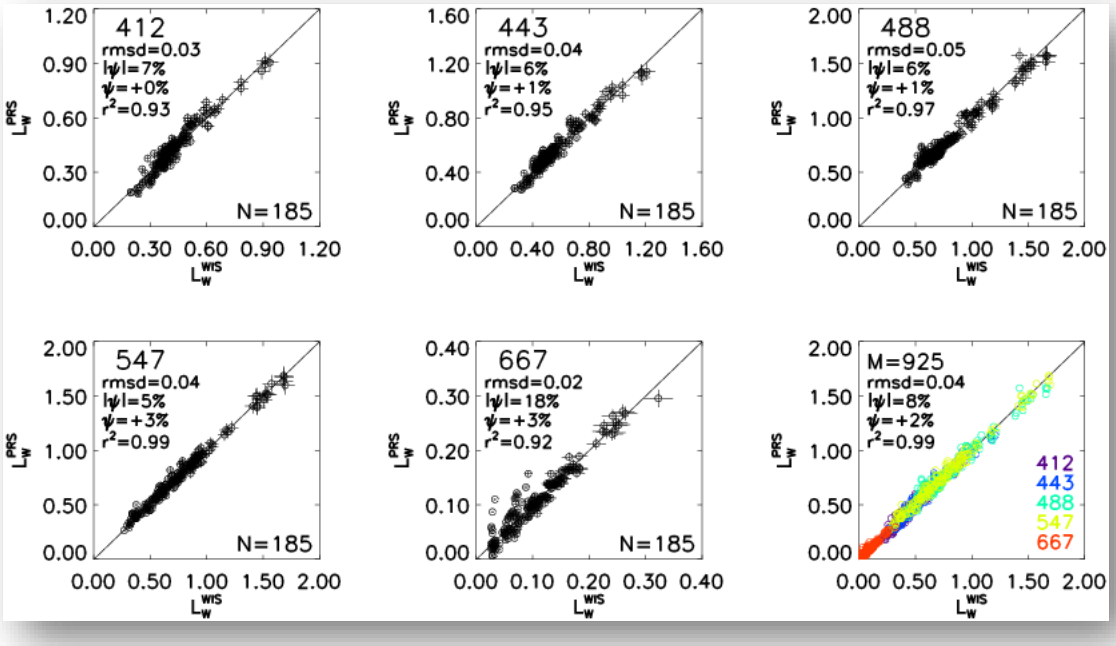

Figure 19. $L_W(\lambda)$ data from above-water radiometric measurements performed in moderately optically complex waters, corrected for the non-nadir view applying the *Chla*-based approach, plotted with respect to coincident $L_W(\lambda)$ data determined with an in-water radiometer system (reprinted from Zibordi, 2015).

This empirical approach definitively violates the basic principle governing the theoretical determination of ρ-factors, which implies that the ρ-factors should represent average sea surface reflectance conditions and consequently should statistically account for any sun- and sky-glint contribution impinging the field-of-view of the L_T sensor. This consideration suggests that the above filtering process may lead to an overcorrection of sky-glint perturbations with a consequent underestimation of $L_w(\lambda)$. In fact, recalling that data are quality-screened for sun-glint and foam contaminations, the use of the average of the lowest radiance values instead of the simple average of all values performed by the L_T sensor, leads to an underestimate of $L_T(\lambda)$ implying an underestimate of $L_w(\lambda)$. Still, the former processing solutions were shown very effective under various observation conditions including measurements collected with diverse field radiometers, and led to extraordinary agreement between above- and in-water radiometric data products (see Fig. 19).

These apparently conflicting results remained unexplained until recent investigations showing: some underestimate of the ρ-factors from Mobley (1999) as detailed in D'Alimonte *et al.* (2021); an already anticipated spectral dependence of the ρ-factors, but ignored when applying the ρ-factors from Mobley (1999); and finally, the introduction of spectral biases in any $L_w(\lambda)$ corrected for the non-nadir view of above-water sensors using approaches not suitable for the specific marine optical properties characterizing the field measurements. Further ongoing investigations on ρ-factors are thus expected to suggests revisions of the filtering solution discussed above (see Zibordi et al. 2025).

Successive quality control steps should flag questionable $L_{WN}(\lambda)$ spectra. These could include the application of empirical thresholds: *e.g.*, $L_{WN}(\lambda) > -0.01$ $mW\ cm^{-2}\ \mu m^{-1}\ sr^{-1}$ indicating absence of exceedingly negative values at any λ; $L_{WN}(400) < L_{WN}(412)$ indicating the lack of consistency between spectral bands for measurements performed in optically complex waters; $L_{WN}(1020) < 0.1$ $mW\ cm^{-2}\ \mu m^{-1}\ sr^{-1}$, except for sites exhibiting very turbid waters, to exclude measurements appreciably affected by the presence of obstacles in the sight of the sea-viewing sensor.

Finally, it would be important to verify the consistency of $L_{WN}(\lambda)$ data with respect to already quality controlled data. This would help identifying those spectra not statistically represented in a reference data set. Clearly, any underrepresented or novel spectrum could suggest measurement issues. An additional and desirable quality control test is that assessing the stability of $L_{WN}(\lambda)$ data over successive measurements. This information is valuable to restrict the validation of satellite data products to measurement conditions characterized by relatively high temporal stability.

Examples of relative- and temporal-consistency tests are provided in Fig.s 20 and 22. The candidate spectrum (*i.e.*, that going to be evaluated) is statistically compared with prototype (*i.e.*, reference) spectra constructed by *i*. averaging already quality controlled spectra exhibiting features similar to the candidate; and *ii*. averaging spectra temporally close (*i.e.*, within minutes) to the candidate.

The example provided in Fig. 20 shows the candidate spectrum satisfying both the relative- and temporal-consistency tests. Conversely, the example in Fig. 21 shows the candidate failing the temporal-consistency test: the candidate L_{WN} spectrum does not pass the temporal-consistency test at the single 400 *nm* centre-wavelength as illustrated by the $L_{WN}(\lambda)$ time series displayed in Fig. 22. Specifically, the candidate spectrum identified by the vertical bar in Fig. 22, shows the value at 400 *nm* deviating from the temporal trend of the close-by data. This spectral deviation affecting a single spectral band is largely explained by the asynchronous spectral acquisition of N_T measurements performed by AERONET-OC radiometers (Zibordi *et al.* 2021).

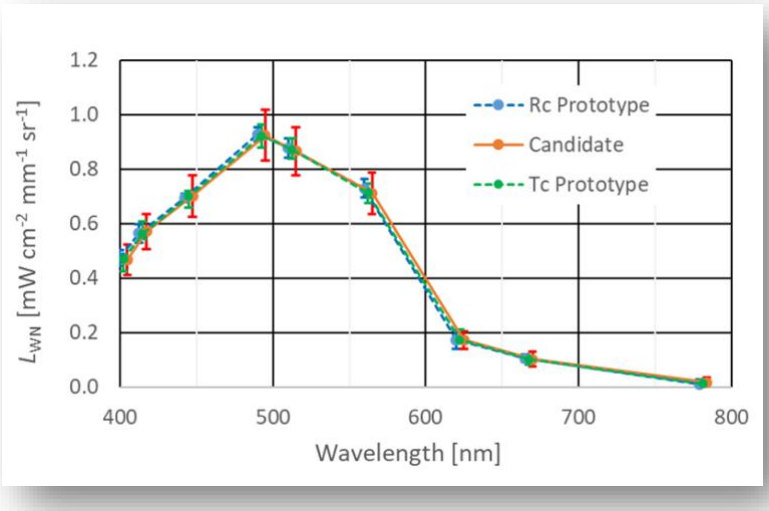

Figure 20. Comparison of $L_{WN}(\lambda)$ candidate and prototype spectra applied for the relative- and temporal-consistency tests, indicated by Rc and Tc, respectively (sample from the AAOT of 20-07-2019 at 12:59:27). The error bars indicate: two times the uncertainty $u_C(\lambda)$ determined for the candidate (*i.e.*, $2 \cdot u_C(\lambda)$); two times the standard deviation of the spectra contributing to the construction of the prototype for the relative-consistency test (*i.e.*, $2 \cdot \sigma_{R_C}(\lambda)$); and two times the standard deviation of the spectra contributing to the construction of the prototype for the temporal-consistency test (*i.e.*, $2 \cdot \sigma_{T_C}(\lambda)$, reprinted form Zibordi *et al.* 2021).

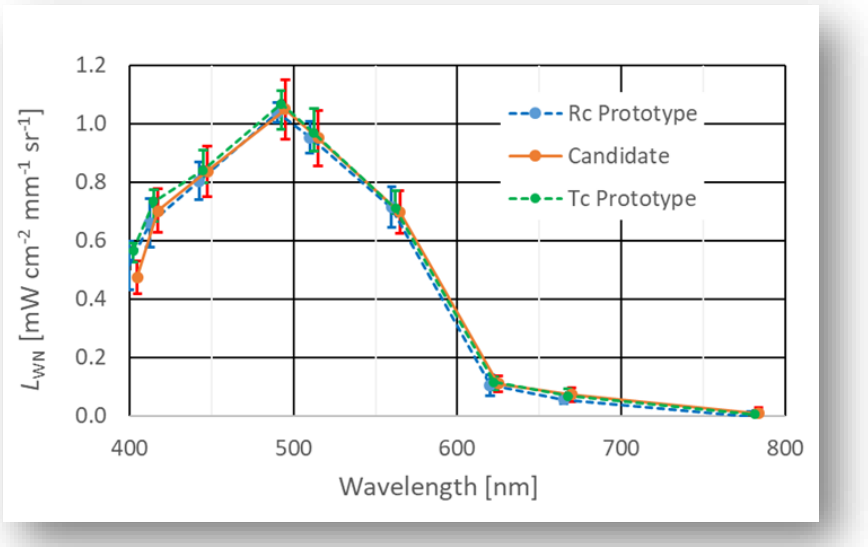

Figure 21. Comparison of $L_{WN}(\lambda)$ candidate and prototype spectra applied for the relative- and temporal-consistency tests, indicated by Rc and Tc, respectively (sample from AAOT of 21-08-2018 at 10:00:47; reprinted form Zibordi *et al.* 2021).

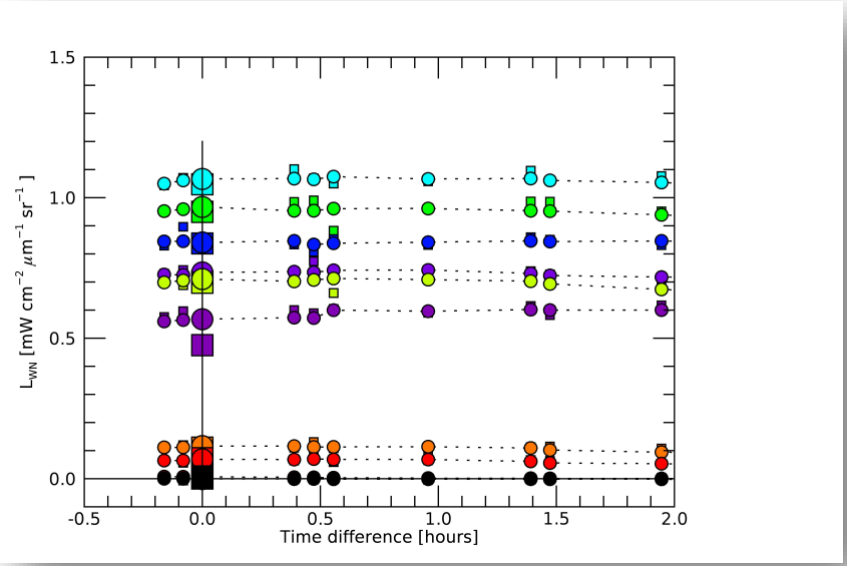

Figure 22. Comparison of $L_{WN}(\lambda)$ candidate and temporal-consistency time-series (sample from AAOT of 21-08-2018 at 10:00:47). The filled squares indicate actual $L_{WN}(\lambda)$ data while filled circles indicate smoothed $L_{WN}(\lambda)$ values. Colours from cyan to black indicate centre-wavelengths from 400 to 670 nm. The vertical bar highlights the L_{WN} candidate spectrum exhibiting temporal inconsistency at 400 nm (the enlarged cyan filled square) (reprinted from Zibordi *et al.* 2021).

14 On uncertainties, with a practical view to their quantification

The term *error* indicates differences between values of measured quantities and the true values of measurands (*i.e.*, the quantity intended to be measured). Errors are unknown and when known, should be corrected. Errors may perturb measurements through *i*. systematic (*i.e.*, consistent) effects due to lack of accuracy, and *ii*. random (*i.e.,* non-replicable) effects due to lack of precision. The detection of systematic errors is quite challenging: it implies the truthful knowledge of full measuring chain encompassing instruments characteristics, and measurement and data handling protocols.

The term *uncertainty* indicates the incomplete knowledge of the measurand through the available information. Therefore, *a measurement of any kind is incomplete unless accompanied with an estimate of the uncertainty associated with that measurement* (Palmer *and* Grant 2010).

Uncertainties are generally divided into type A when determined through statistical methods (*e.g.*, multiple measurements allowing to quantify standard deviations) and type B when determined by means other than statistical (*e.g.,* models, published data, calibration certificates, or even experience). Uncertainties can be additive (*i.e.,* independent of the measured value such as the inaccurate quantification of the dark signal) or multiplicative (*i.e.,* dependent on the measured value such as that related to the inaccurate determination of the responsivity of the radiometer). Assuming individual uncertainty contributions are independent, multiplicative and normally distributed, the overall measurement uncertainty is given by their combined values (*i.e.,* the square root of the sum of their squared values). The so called coverage factor k (Johnson *et al.* 2014) determines the level of confidence on uncertainties: k = 1, 2 and 3 refer to confidence levels of approximately 68%, 95% and 99%, respectively, related to one, two and three standard deviations.

Uncertainties, when possible, should be provided in both relative (*i.e.,* %) and physical units. The range of values for which the uncertainties are proposed should also be reported together with details on measurement conditions. In fact, uncertainties determined for a specific range of values may not necessarily be the same for other ranges or different measurement conditions.

The quantification of uncertainties of *in situ* measurements should comprehensively address contributions from the calibration source and its transfer, the non-ideal performance of the radiometer and of any model applied for data reduction, the impact of environmental variability, and perturbations by instruments housing (*i.e.,* self-shading characteristic of in-water measurements) and by deployment platforms.

Many publications mention a *5%* uncertainty target for both satellite and *in situ* radiometric data. It is worth looking how this uncertainty target was conceived (see also Zibordi and Voss, 2014). An uncertainty of 5% was originally defined for satellite derived $L_{WN}(\lambda)$ in the blue spectral region to satisfy the 35% uncertainty in chlorophyll-*a* concentration determined by an existing bio-optical algorithm proposed for oligotrophic waters (Gordon and Clark 1981). The 5% uncertainty value was then set as the target for $L_{WN}(\lambda)$ for the majority of ocean colour missions, regardless of the spectral regions and applications. This uncertainty assigned to satellite derived $L_{WN}(\lambda)$ unavoidably prompted the need for uncertainties better than 5% for *in situ* $L_{WN}(\lambda)$. This implies the need to constrain individual sources of uncertainty of *in situ* radiometric data to within 1-2%, which is commonly referred as 1*% radiometry* (McClain *et al*. 2007). It is important, however, to appreciate that this uncertainty target is only applicable to oligotrophic and likely mesotrophic open sea waters in the blue-green spectral regions. Conversely, in optically complex waters the uncertainties affecting both satellite and *in situ* derived radiometric products may largely exceed the 5% target and are matter of ongoing discussions.

The Guide on Measurement Uncertainties (GUM, JCGM 2008) provides a general metrological framework for the quantification of measurement uncertainties. The standard uncertainty associated with a measurand indirectly determined from other quantities through a measurement model $y = f(x_1, \ldots, x_N)$, can be obtained propagating the uncertainties of each model input quantity through the first-order expansion of Taylor series:

$$\tilde{u}_c^2(y) = \sum_{i=1}^{N} \left(\frac{\partial f}{\partial x_i}\right)^2 u^2(x_i). \tag{9}$$

The above equation may be further expanded to account for non-negligible correlations between pairs of input quantities x_i, x_j or non-linearity in the model function of the measurement model (see Cazzaniga *and* Zibordi 2023). For simplicity, excluding correlations and non-linearity contributions, the combined uncertainty $\tilde{u}_c(L_W)$ for the spectral values of L_W are quantifiable from the individual uncertainties of L_T, L_i and ρ (hereafter indicated by $u(L_T)$, $u(L_i)$ and $u(\rho)$, respectively), according to

$$\tilde{u}_c^2(L_W) = u^2(L_T) + u^2(L_i)\rho^2 + u^2(\rho){L_i}^2\,. \tag{10}$$

With reference to Eq. (10), the value of $u_c(L_{WN})$ is then quantifiable considering the additional uncertainties of C_Q and C_A, hereafter defined as $u(C_Q)$ and $u(C_A)$, respectively,

$$\tilde{u}_c^2(L_{WN}) = (C_Q C_A)^2 \tilde{u}_c^2(L_W) + (L_W C_A)^2\, u^2(C_Q) + (L_W C_Q)^2\, u^2(C_A). \tag{11}$$

Gergely and Zibordi (2014) and successively Cazzaniga *and* Zibordi (2023), applied GUM to investigate the uncertainties affecting the values of L_{WN} determined from multispectral above-water-measurements (*i.e.*, AERONET-OC systems relying on a single radiometer for L_T and L_i measurements, and the theoretical determination of E_s). Their analysis showed that Eq. (10) provides a conservative estimate of uncertainties, which does not much differ from the combined uncertainties determined considering the simple quadrature sum of the independent and multiplicative contributions $u_1(L_{WN}), u_2(L_{WN}), \ldots, u_j(L_{WN})$ to L_{WN}, according to

$$u(L_{WN}) = \sqrt{[u_1(L_{WN})]^2 + [u_2(L_{WN})]^2 + \cdots + [u_j(L_{WN})]^2}. \tag{12}$$

Table 4 provides an example of L_{WN} uncertainty contributions quantified with Eq. (12) expressed in relative terms (*i.e.*, in percent of $u(L_{WN})/L_{WN}$) at the 443, 551 and 665 *nm* centre-wavelengths accounting for:

i. uncertainty of the absolute calibration of the L_i and L_T sensors due to specific contributions from an FEL irradiance standard lamp, reflectance plaque, and mechanical positioning of the various components:
ii. uncertainty due sensor *sensitivity change* between successive calibrations;
iii. uncertainty in the *corrections* for bidirectional effects computed as 25% of the applied correction coefficients;
iv. uncertainty in the determination of t_d used to estimate E_s;
v. uncertainty in the determination of ρ due to wave effects and data filtering during processing;
vi. uncertainty in the value of W; and
vii. uncertainties due to *environmental effects*.

Table 4. Individual contributions (in percent) to the $L_{WN}(\lambda)$ combined uncertainties determined for measurements performed in moderately optically complex waters at the centre-wavelengths 443, 551 and 667 *nm* (after Zibordi 2009).

Source	443	551	667
Absolute calibration	2.1	2.1	2.1
Sensitivity change	0.2	0.2	0.2
Correction	2.0	2.9	1.9
t_d	1.5	1.5	1.5
ρ	1.3	0.6	2.5
W	0.8	0.4	0.4
Environmental effects	2.1	2.1	6.4
Combined values	**4.2**	**4.5**	**7.6**

As already anticipated, the values provided in Table 4 were largely confirmed by the work of Gergely and Zibordi (2014) and Cazzaniga *and* Zibordi (2023), who rigorously applied GUM to quantify the uncertainties for the same data, measurement method and data reduction scheme. It is specified that their analysis benefitted of measurements performed with multispectral instruments not exhibiting appreciable dependence on temperature, non-linearity, stray light and polarization (Zibordi *et al.* 2021). An equivalent almost ideal instrument performance is commonly not extendable to optical radiometers with gratings, lenses or mirrors. An attempt to illustrate the impact of such a non-ideal performance is provided in Table 5. In particular, in addition to the uncertainty contributions already included in Table 4, the new Table 5 provides estimate of biases (highlighted in red) tentatively accounting for the perturbing effects of the non-ideal performance of a conjectural instrument. These biases (*i.e.*, hypothetical *errors*, *not uncertainties*) are proposed for the temperature response (assuming a variation of 10°C with respect to the calibration temperature), polarization sensitivity, stray light effects and non-linearity. The biases (*i.e.*, $\varepsilon_1(L_{WN}), \varepsilon_2(L_{WN}), \dots, \varepsilon_i(L_{WN})$) and the uncertainties (*i.e.*, $u_1(L_{WN}), u_2(L_{WN}), \dots, u_j(L_{WN})$) are then combined according to

$$u(L_{WN}) = \sqrt{[\varepsilon_1(L_{WN}) + \varepsilon_2(L_{WN}) + \cdots + \varepsilon_i(L_{WN})]^2 + [u_1(L_{WN})]^2 + [u_2(L_{WN})]^2 + \cdots + [u_j(L_{WN})]^2} \qquad (13)$$

which implies that biases contribute to the final values of $u(L_{WN})$ with their sign.

Results in Table 5, again expressed in relative terms (*i.e.*, in percent of $u(L_{WN})/L_{WN}$), exhibit differences in the combined value $u(\lambda)$ with respect to those provided in Table 4: still these changes are minor. This is explained by the relatively small values of the biases, and by the fact they are considered with their sign which naturally allows for compensations.

Table 5. Re-visitation of the $L_{WN}(\lambda)$ relative uncertainties provided in Table 4 for the centre-wavelengths 443, 551 and 667 *nm* accounting for biases due to hypothetical radiometer temperature response, polarization sensitivity, stray-light effects and non-linearity (all highlighted in red) typical of a series of actual hyperspectral radiometers.

Source	443	551	667
Absolute calibration	2.1	2.1	2.1
Sensitivity change	0.2	0.2	0.2
Correction	2.0	2.9	1.9
Temperature response (+10 ℃)	**+0.4**	**−0.6**	**−1.4**
Polarization Sensitivity	**+0.1**	**+0.2**	**+0.4**
Stray-light effects	**−1.0**	**+0.5**	**+0.5**
Nonlinearity	**−0.0**	**−1.0**	**−0.2**
t_d	1.5	1.5	1.5
ρ	1.3	0.6	2.5
W	0.8	0.4	0.4
Environmental effects	2.1	2.1	6.4
Combined values	**4.2**	**4.6**	**7.6**

The above findings should not suggest that ignoring the actual radiometer performances may still lead to an acceptable quantification of the uncertainties. Results simply indicate that the non-ideal radiometer performance, if confidently constrained to within tentative measurement errors (*i.e.*, biases) of ±1%, may still allow to have a first guess on the uncertainties affecting data products. It is, however, fundamental that any potential radiometer non-performance is investigated and estimated, and additionally that comprehensive and accurate quantifications of uncertainties remain a chief objective of the ocean colour community (see Białek *et al*. 2020) .

The uncertainty analysis provided in Gergely *and* Zibordi (2014) and Cazzaniga *and* Zibordi (2023) show that combined uncertainties solely expressed in relative terms (*i.e.*, in %) may provide incomplete information. In fact, measurements exhibiting larger relative uncertainties for a specific water type with respect to others, may actually have lower absolute uncertainties. This suggests that uncertainties should be provided in absolute and relative terms when their quantification is expected to impact the final assessment of data products or become a reference for the community.

Gergely *and* Zibordi (2014) and Cazzaniga *and* Zibordi (2023) documented how combined uncertainties may largely vary across different geographic regions as a result of the diverse $L_{WN}(\lambda)$ spectra. An example of such dependence is shown in Table 6 for oligotrophic and optically complex waters.

Finally, additional important element emerging from the work of Cazzaniga *and* Zibordi (2023) already evident in Table 4, is a further confirmation that the uncertainty contributions due to the ρ-factor and environmental variability are those most affecting the uncertainty budget (see Fig. 23).

Table 6. Relative uncertainties (in percent) determined at several centre-wavelengths (in units of *nm*) for $L_{WN}(\lambda)$ from oligotrophic waters and alternatively from optically complex waters dominated by coloured dissolved organic matter (after Cazzaniga *and* Zibordi 2023).

Relative uncertainty	**400**	**412**	**443**	**490**	**510**	**560**	**620**	**667**
$u_{c,mj}^{IOP}/L_{WN}$ (oligotrophic waters)	5.1	4.8	4.4	4.0	4.0	4.1	5.5	6.2
$u_{c,mj}^{IOP}/L_{WN}$ (optically complex waters)	22.3	18.7	11.1	5.9	5.1	4.5	5.8	6.7

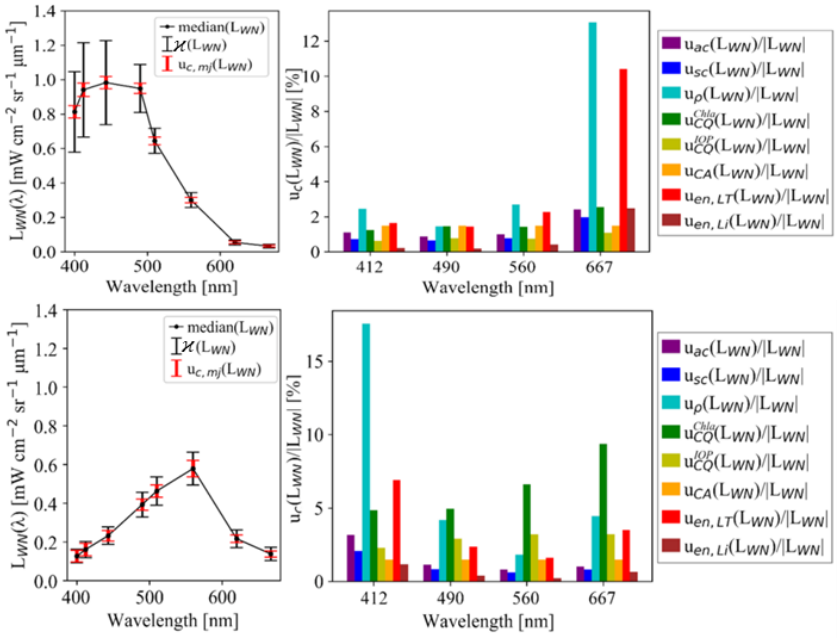

Figure 23. Relative uncertainties affecting AERONET-OC $L_{WN}(\lambda)$ from diverse water-types: oligotrophic waters in the Western Mediterranean Sea (upper panels) and optically complex waters dominated by coloured dissolved organic matter in the Baltic Sea (lower panels). The panels in the left column display the median $L_{WN}(\lambda)$ spectra for the two regions together with their median absolute deviations ($\varkappa$) and uncertainty estimates only accounting for major correlations ($u_{c,mj}$). The panels in the right column display the contributions in percent determined for the various sources of uncertainty: absolute radiometric calibration, u_{ac}; sensitivity change during deployments, u_{sc}; ρ-factor, u_{ρ}; correction for bidirectional effects determined with the *Chla*-approach, u_{CQ}^{Chla}; corrections for bidirectional effects determined with the *IOP*-approach, u_{CQ}^{IOP}; corrections applied for the normalization of L_W for illumination conditions, u_{CA}; environmental perturbation in L_T, $u_{en,LT}$; environmental perturbations in L_i, $u_{en,Li}$ (reprinted from Cazzaniga *and* Zibordi 2023).

15 On requirements for field inter-comparisons

Inter-comparisons are natural means to investigate differences across measurement methods, instruments performance and data processing solutions. Literature presents a large number of radiometric inter-comparisons sometime supported by questionable assumptions and often leading to dubious conclusions. The most debatable assumption is that differences among independent measurements provide an estimate for uncertainties. Differences and uncertainties are not equivalent: differences need to be justified by uncertainties. In fact, differences may result from the compensation of errors (unknown biases) due to the non-ideal performance of instruments, or mistakes and approximations in the implementation of measurement methods or processing. As a basic example, biases between calibration coefficients (still explained by calibration uncertainties) for independent systems not benefitting of laboratory inter-calibrations, may contribute to the compensation of differences resulting from the adoption of diverse measurement procedures or processing solutions. Because of this, together with consistent absolute radiometric calibrations ideally obtained through laboratory inter-calibrations, also comprehensive characterizations of the instruments contributing to inter-comparisons are essential. Further, the determination of uncertainty budgets for any inter-compared data product is fundamental. These budgets should be determined following metrology principles by accounting for any potential source of uncertainty. Because of this, field inter-comparisons should be designed avoiding any uncertainty source for which a value cannot be assigned. A typical case is offered by the perturbations originated by deployment structures (*e.g.*, ships or towers). If these cannot be avoided or accurately quantified accounting for the mutual sensor-structure position, an effort should be made to ensure their minimization and equivalent contribution to any inter-compared quantity. Clearly, any error affecting the determination of the final data product, impacts the accuracy of the product itself. Diverse biases affecting the determination of inter-compared data products may enhance or reduce their difference regardless of any quantified uncertainty. Because of this, diverse uncorrected biases affecting inter-compared data would prevent to distil sound conclusions on instruments performance, measurement methods or data processing.

Building on previous considerations, any field inter-comparison aiming at investigating measurement methods, instruments performance or alternative data processing, should rely on data collected fulfilling the following basic principles:

- The instruments (*i.e.,* radiometers) have a recent absolute SI traceable calibration and their non-ideal performances are known as a result of comprehensive characterizations.
- Measurement methods and the related quality assurance criteria are fully valued and their implementation was ideally matter of independent verifications.
- Processing solutions and quality control criteria are also fully appreciated, implemented and ideally supported by independent verifications.
- Potential sources of errors (*i.e.*, unquantifiable biases) are minimized or least made equivalent across the inter-compared measurements.
- Uncertainties are quantified and inter-comparisons are carried out in agreement with metrology principles.

On the latter point it should be considered that differences between inter-compared quantities (*e.g.,* $L^A_{WN,\,i}(\lambda) - L^B_{WN,\,i}(\lambda)$) from systems/methods *A* and *B*, should be supported by the following equation when assuming negligible correlations between uncertainties:

$$\left[L^A_{WN,\,i}(\lambda) - L^B_{WN,\,i}(\lambda)\right]^2 < k\left[u^2_{A,\,i}(\lambda) + u^2_{B,\,i}(\lambda) + v^2_{A,\,i}(\lambda) + v^2_{B,\,i}\right] \tag{14}$$

where *i* indicates the matchup index, *k* is the coverage factor, $u_{A,i}(\lambda)$ is the expected uncertainty for data from the instrument/method *A*, $u_{B,i}(\lambda)$ is the uncertainty for data from the instrument/method *B*, and, $v_{A,i}(\lambda)$ and $v_{B,i}(\lambda)$ the uncertainties due spatio-temporal changes affecting *A* and *B* data.

Taking *k*=1 and assuming that most of the major contributions to differences are accounted by $u_{A,i}(\lambda), u_{B,i}(\lambda), v_{A,i}(\lambda), v_{B,i}(\lambda)$, the uncertainty-normalized difference for each data pair and λ is given by:

$$\varepsilon_i(\lambda) = \frac{L^A_{WN,\,i}(\lambda) - L^B_{WN,\,i}(\lambda)}{\sqrt{u^2_{A,\,i}(\lambda) + u^2_{B,\,i}(\lambda) + v^2_{A,\,i}(\lambda) + v^2_{B,\,i}(\lambda)}}. \tag{15}$$

In agreement with Hunt *et al.* (2020) and following Zibordi *et al.* (2022), if $u_{A,i}(\lambda), u_{B,i}(\lambda), v_{A,i}(\lambda), v_{B,i}(\lambda)$ well describe the variance of the difference $L^A_{WN,i}(\lambda) - L^B_{WN,i}(\lambda)$, the probability distribution of the $\varepsilon_i(\lambda)$ values is standard normal and consequently centered at 0 with standard deviation $\sigma(\varepsilon_i) = 1$. If the uncertainty values are underestimated, the distribution of $\varepsilon_i(\lambda)$ would exhibit $\sigma(\varepsilon_i) > 1$. On the contrary, if the uncertainty values are overestimated, the distribution of $\varepsilon_i(\lambda)$ would give $\sigma(\varepsilon_i) < 1$. Additionally, when the distribution of $\varepsilon_i(\lambda)$ is not centered at 0 and consequently exhibits a bias, a distribution mean $\mu(\varepsilon_i) < \pm 1$ would still indicate the bias is somehow represented by the uncertainty values.

16 On data archival, access and re-processing

Equivalent to the data structure already endorsed by existing measurement programs, data should be archived at incremental quality levels. For instance Level 0 should include only raw data from reliable measurement sequences together with absolute radiometric calibration coefficients, characterization factors, any ancillary data and metadata, necessary for successive processing. Level 1 should include $L_i(\theta',\phi,\lambda)$ and $L_T(\theta,\phi,\lambda)$ calibrated values already satisfying relevant quality control tests. Finally Level 2 should comprise fully quality controlled $L_{WN}(\lambda)$ data. These latter data, should also satisfy consistency between pre- and post-deployment calibration coefficients, which should exhibit differences smaller than tentatively 2%.

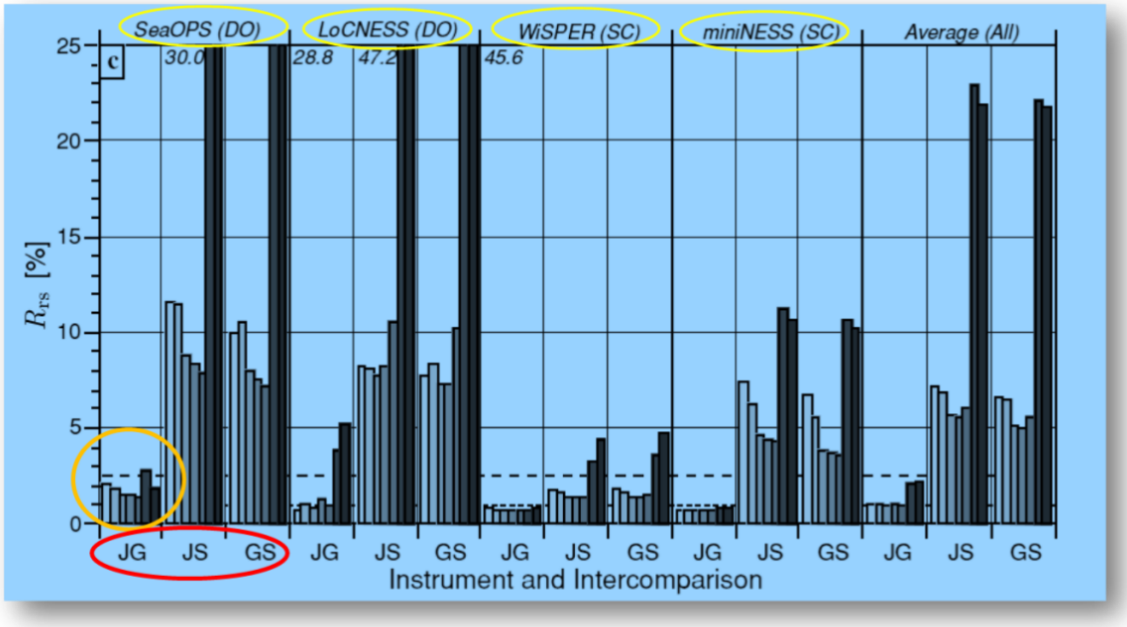

Figure 24. Percent differences in spectral $R_{RS}(\lambda)$ resulting from the application of three independent codes (still, inspired by the same protocol) to the processing of diverse in-water profiles from different radiometer systems operated in various water types. J, G and S indicate the diverse processors. Each sub-panel in the figure, which is associated to data from a specific optical profiler (*i.e.*, *SeaOPS*, *LoCNESS*, *WiSPER*, *miniNESS*), shows the percent differences for pairs of processors (*i.e.*, JG, JS and GS) through histograms whose grey levels identify different spectral bands from the blue to the red (redrawn from Hooker *et al.* 2001).

Reprocessing of data often suggested by advances in methods and instruments re-calibration, is a fundamental need for any relevant measurement program. This should be favoured by an effective organization of measurements, ancillary data and details on instruments absolute radiometric calibration and characterizations. In terms of processing strategy, the adoption of centralized data processors would help reducing inconsistencies intrinsic of the application of independent data reduction codes. Still, it is emphasized the importance of throughout assessments of processing codes through benchmarking. In fact, equivalent to the need for verifying the performance of calibration facilities through the inter-calibration of instruments, also code inter-comparisons are essential exercises to identify issues in protocols implementation.

The example provided in Fig. 24, clearly shows challenges in reaching agreement in data products from different processors applied to a variety of in-water radiometric profiles from diverse marine regions, regardless of the ideal adoption of the same processing protocol. Results (see details in Hooker *et al.* 2002) suggest that diverse processing implementations, also applicable to above-water radiometry, may become the source of unexpected errors.

Finally, timely and open access to data products is ultimately a fundamental need for any validation program. Because of this, in addition to the need for establishing, maintaining and continuously expanding repositories beyond any specific mission life, care should be put in imposing fair data policies facilitating access to data, but also granting recognition to data providers.

17 On the application of field data to the assessment of satellite data products

The assessment of the accuracy of satellite data products through independent data, generally relies on field data with declared uncertainties. This section addresses the application of *in situ* $L_{WN}^{PRS}(\lambda)$ from the Ocean Colour component of the Aerosol Robotic Network (AERONET-OC) to assess $L_{WN}^{OLCI-A}(\lambda)$ products from the Ocean and Land Colour Instrument on-

board the Sentinel 3A satellite (here after labelled as *OLCI-A*). The assessment is performed through the direct comparison of satellite and *in situ* data match-ups (*i.e.*, spectrally, spatially and temporally matching data).

Spectral differences between remote sensing and *in situ* data should be minimized by determining synthetic $L_{WN}^{PRS}(\lambda)$ at the specific centre-wavelength λ of interest from $L_{WN}^{PRS}(\lambda_0)$ determined using measurements performed at the nearest centre-wavelength λ_0. Assuming ideal (square) 10 nm wide spectral band passes, a solution is offered by the band-shifting scheme proposed in Zibordi *et al.* (2006) with

$$L_{WN}^{PRS}(\lambda) = L_{WN}^{PRS}(\lambda_0) \left(\frac{E_0(\lambda)\, f(\lambda)\, \mathrm{Q}(\lambda_0)}{\mathrm{E}_0(\lambda_0)\, \mathrm{Q}(\lambda)\, f(\lambda_0)} \frac{b_b(\lambda)}{\mathrm{a}(\lambda) + b_b(\lambda)} \frac{\mathrm{a}(\lambda_0) + b_b(\lambda_0)}{b_b(\lambda_0)} \right) \tag{16}$$

where f is the function relating the irradiance reflectance to the seawater inherent optical properties and Q describes the anisotropic distribution of the in−water light field (Morel *et al*. 2002), a is the total seawater absorption coefficient given by the sum of the absorption coefficients of particulate matter, a_p, colored dissolved organic matter, a_y, and pure seawater, a_w; and b_b is the seawater backscattering coefficient given by the sum of the backscattering coefficients of particulate matter, b_{bp}, and pure seawater, b_{bw}.

Synthetic values of $L_{WN}^{PRS}(\lambda)$ can be computed:

i. assuming λ is close to λ_0 so that $f(\lambda)/Q(\lambda) \times Q(\lambda_0)/f(\lambda_0) \approx 1$, and ;

ii. a and b_{bp} iteratively determined with regional bio-algorithms or inversion schemes applied to $L_{WN}^{PRS}(\lambda)$.

It is however acknowledged that the above approach is affected by uncertainties increasing with the distance between λ and λ_0. Because of this, by relying on a comprehensive data set of simulated spectra, an alternative approach has been proposed to re-construct hyperspectral remote sensing reflectance R_{rs} data from multispectral ones (see Talone *et al.* 2024). The performance of this reconstruction scheme has been verified in the 400-700 nm interval for hyperspectral data from the Ocean Color Instrument (OCI) using R_{rs} at the AERONET-OC visible centre wavelengths. Results indicated the potential for reconstructing OCI spectra within +/-2% across large portions of the visible spectrum.

Matchups are constructed applying satellite extraction protocols, which may exhibit differences and naturally lead to appreciable differences (Concha *et al.* 2021). Matchups can be confidently constructed using the median of the 3×3 satellite pixels centred at various measurement sites and applying criteria to maximize the *comparability* of satellite and *in situ* data. In the example provided here for *OLCI-A* radiometric data (Baseline Collection OL_L2M_003.01), matchups have been retained for successive analysis when: *i*. the time difference Δt between *in situ* measurement and satellite overpass is less than ±2 hr (only retaining the *in situ* data closest in time to the satellite overpass); *ii*. none of the 3×3 pixels is affected by the standard processing flags; *iii*. the coefficient of variation (*i.e.*, the ratio of standard deviation to mean) of $L_{WN}^{OLCI-A}(\lambda)$ is lower than 20% at 560 nm for the nine pixels (the 560 nm centre-wavelength is expected to exhibit a lower dependence on optically significant constituents and surface perturbations with respect to the other centre-wavelengths in the visible portion of the spectrum); *iv*. the viewing angle is lower than 60°; *v*. the sun zenith angle is lower than 70°; and *vi*. the aerosol optical depth τ_a determined at a near-infrared centre-wavelength (*i.e.*, 865 nm) is lower than 0.5 in view of avoiding data affected by cloud perturbations.

The analyses have been generally restricted to $L_{WN}(\lambda)$ at centre-wavelengths λ comprised between 400 to 700 nm. Assessments at longer centre-wavelengths have been considered of little relevance because of the relatively large uncertainties affecting $L_{WN}^{PRS}(\lambda)$ in the near-infrared spectral bands (Zibordi *et al.* 2021).

Satellite data products can be evaluated through both qualitative and quantitative comparisons. The first aims at visualizing artefacts that may characterize satellite or even *in situ* data. Conversely the second relies on statistical indices for the N matchups of satellite (*OLCI-A*) and *in situ* (*PRS*) data $[(\Im_1^{OLCI-A}, \Im_2^{OLCI-A}, \ldots, \Im_N^{OLCI-A}), (\Im_1^{PRS}, \Im_2^{PRS}, \ldots, \Im_N^{PRS})]$ where $\Im$ is the compared quantity (*i.e.*, $L_{WN}(\lambda)$), and the subscripts 1, 2 …, N indicate the matchup index. Considered statistical indices are: the median of differences Δ_m and the median of absolute (unsigned) differences $|\Delta|_m$; the median of relative differences ψ_m and the median of absolute (unsigned) relative differences $|\psi|_m$, both determined with respect to the *in situ* reference data; the root mean square of differences *rmsd*; and the determination coefficient r^2 from data regression.

The indices $|\Delta|_m$ and $|\psi|_m$ provide hints on the dispersion of data, conversely Δ_m and ψ_m provide information on biases. The quantities $|\psi|_m$ and ψ_m are expressed in percent and provide an immediate view on the comparison. On the contrary, $|\Delta|_m$, Δ_m and *rmsd* are in physical units (*e.g., mW cm*$^{-2}$ *μm*$^{-1}$ *sr*$^{-1}$) and complement the comparison with statistical indices strictly related to the values and range of the assessed $L_{WN}(\lambda)$.

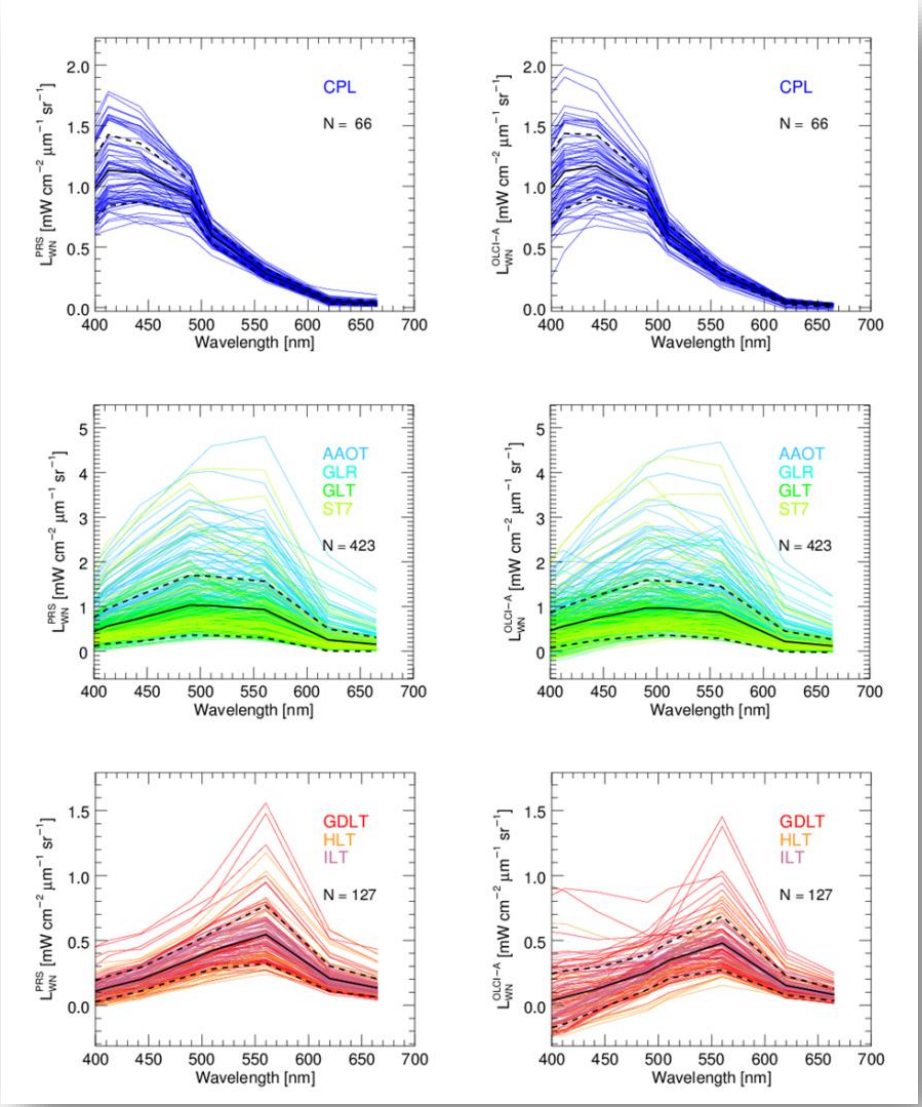

Figure 25. Qualitative comparison of AERONET-OC $L_{WN}^{PRS}(\lambda)$ (left column) and OLCI-A $L_{WN}^{OLCI-A}(\lambda)$ (right column) spectra for different water types: oligotrophic-mesotrophic in the first row of panels (*i.e.*, CPL site); optically complex in the second row of panels (*i.e.*, AAOT, GLR, GLT, ST7 sites); and optically complex, but dominated by high concentrations of CDOM in the last row of panels (*i.e.*, GDLT, HLT and ILT sites). The continuous black lines indicate median values while the dashed black lines indicate ± 1 σ (reprinted from Zibordi *et al.* 2022).

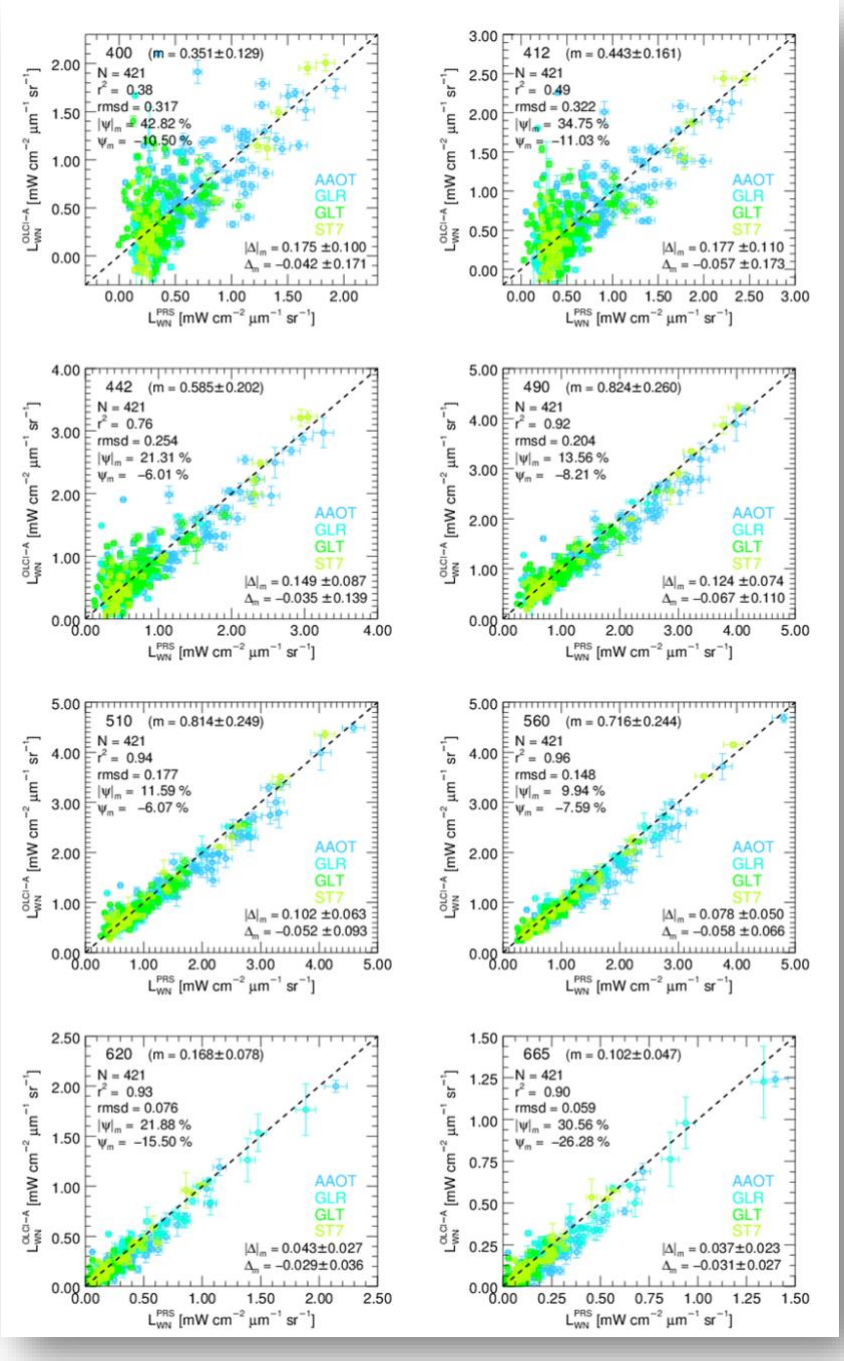

Figure 26. Scatter plots of OLCI-A $L_{WN}^{OLCI-A}(\lambda)$ versus AERONET-OC $L_{WN}^{PRS}(\lambda)$ data for the optically complex waters occurring at the AAOT, GLR, GLT and ST7 sites, for the 400, 412, 442, 490, 510, 560, 620 and 665 nm centre-wavelengths. The error bars associated with the *in situ* data indicate measurement uncertainties while those related to satellite data indicate the variation coefficient determined from the 3×3 pixels contributing to matchups. N indicates the number of matchups, r^2 the determination coefficient, *rmsd* the root-mean square of differences, $|\psi|_m$ the median of unsigned percent differences, ψ_m the median of percent differences, $|\Delta|_m$ the median of unsigned differences and Δ_m the median of differences. The ± values associated with $|\Delta|_m$ and Δ_m are the median absolute deviation $\varkappa$. The values in brackets aside the centre-wavelength at the top of each panel, indicate the median m ± the related median absolute deviation $\varkappa$ of $L_{WN}^{PRS}(\lambda)$ at the specific centre-wavelength λ (reprinted from Zibordi *et al.* 2022).

When considering that the $L_{WN}(\lambda)$ values may not exhibit normal distribution, the use of the *median* with respect to the *mean* allows to better determining the *centrality* of the comparison results. Additionally, the impact of outliers is minimized by determining $|\psi|_m$ and ψ_m by excluding values exceeding two standard deviations from the mean. It is however noted that this filtering solution is only effective with a relatively low number of matchups.

The qualitative comparison of matchup spectra shown in Fig. 25 already provides general indication on the consistency of the reference AERONET-OC $L_{WN}^{PRS}(\lambda)$ data across the various sites with spectra well representative of oligotrophic waters, complex waters exhibiting various concentrations of optically significant materials and finally waters characterized by a high concentration of coloured dissolved organic matter. Conversely, still exhibiting a general agreement with the *in situ* reference data, OLCI-A $L_{WN}^{OLCI-A}(\lambda)$ spectra show some occasional inconsistency and frequent negative values at the blue centre-wavelengths for the waters dominated by coloured dissolved organic matter. Comprehensive statistical results are provided in Fig. 26 for the sole case of generic optically complex waters. Definitively, the comparison of $L_{WN}^{OLCI-A}(\lambda)$ with $L_{WN}^{PRS}(\lambda)$ shows values of $|\psi|_m$ and ψ_m, and of $|\Delta|_m$ and Δ_m largely varying across the spectral bands. These results, still relying on statistical indices, already provide general indications on the accuracy of satellite data products in terms of scattering and bias with respect to the *in situ* reference data. The comparability of these results with independent studies, which may benefit of alternative *in situ* reference data or simply focus on different geographic regions, are sometime difficult. In fact, many studies do not provide details on the range of the $L_{WN}(\lambda)$ input values. Because of this, at least the median m and the median absolute deviation $\varkappa$ of the *in situ* reference data should be provided for each comparison case. Finally, it is recalled that $\varkappa$ is much less influenced by outliers than σ being a measure of the statistical dispersion of the data points around their *median* with $\varkappa = median[\,|\,(\Im_1, \Im_2, \ldots, \Im_N) - median(\Im_1, \Im_2, \ldots, \Im_N)\,|\,]$ where $\Im_i = \Im_1, \Im_2, \ldots, \Im_N$ indicates the quantities (*e.g.*, the $L_{WN}(\lambda)$ values) included in the comparison, and the subscript i the matchup index.

18 On the application of field data to quantify uncertainties in satellite data products

The direct comparison of satellite versus *in situ* data only provides general indications on the accuracy affecting data products: none of the statistical quantities formerly associated to the comparison is a direct expression of the uncertainties. As a natural step, this section addresses the application of metrology principles to quantify the uncertainties affecting satellite derived data products.

As already anticipated, accuracy requirements for satellite radiometric products are commonly summarized by a spectrally and water-type independent 5% *uncertainty* (*e.g.*, EUMETSAT 2019). This generic 5% *uncertainty* requirement, however, should only apply to oligotrophic/mesotrophic waters in the blue-green spectral region. To assess the fulfilment of such a requirement, radiometric data products from OLCI-A Baseline Collection OL_L2M_003.01 (Zibordi *et al.* 2022) have been evaluated applying the so-called consistency principle: independent measurements of the same quantity should agree within their individual uncertainties (Immler *et al.* 2010, Hunt *et al.* 2020). Following Zibordi *et al.* (2022), by *i.* applying the above principle to satellite $L_{WN,i}^{OLCI-A}(\lambda)$ and *in situ* $L_{WN,i}^{PRS}(\lambda)$ matchups with i indicating the matchup index, *ii.* choosing a coverage factor $k = 1$, and *iii.* assuming negligible correlations between uncertainties, the following relationship should be statistically satisfied:

$$\left[L_{WN,i}^{OLCI-A}(\lambda) - L_{WN,i}^{PRS}(\lambda)\right]^2 < k\left[u_{OLCI-A,i}^2(\lambda) + u_{PRS,i}^2(\lambda) + v_{OLCI-A,i}^2(\lambda) + v_{PRS,i}^2(\lambda)\right] \quad (17)$$

where $u_{OLCI-A,i}(\lambda)$ indicates the expected uncertainty of satellite data, $u_{PRS,i}(\lambda)$ the quantified uncertainty for the *in situ* data and, $v_{OLCI-A,i}(\lambda)$ and $v_{PRS,i}(\lambda)$ the spatio-temporal variabilities affecting satellite and *in situ* data, respectively.

Assuming that most of the major contributions to radiance differences are accounted by $u_{PRS,i}(\lambda)$, $v_{OLCI-A,i}(\lambda)$, $v_{PRS,i}(\lambda)$ and $u_{OLCI-A,i}(\lambda)$, where this latter is unknown, the uncertainty-normalized difference for each data pair and λ is given by

$$\varepsilon_i(\lambda) = \frac{L_{WN,i}^{OLCI-A}(\lambda) - L_{WN,i}^{PRS}(\lambda)}{\sqrt{u_{OLCI-A,i}^2(\lambda) + u_{PRS,i}^2(\lambda) + v_{OLCI-A,i}^2(\lambda) + v_{PRS,i}^2(\lambda)}}. \quad (18)$$

Restating what already written in section *'On requirements for field inter-comparisons'*, if $u_{OLCI-A,i}(\lambda)$, $u_{PRS,i}(\lambda)$, $v_{OLCI-A,i}(\lambda)$, $v_{PRS,i}(\lambda)$ well describe the variance of the difference $L_{WN,i}^{OLCI-A}(\lambda) - L_{WN,i}^{PRS}(\lambda)$, the probability distribution of the $\varepsilon_i(\lambda)$ values would be standard normal and consequently centred at 0 with standard deviation $\sigma(\varepsilon_i(\lambda))$ equal to 1. In the case the uncertainty values are underestimated, the distribution of $\varepsilon_i(\lambda)$ would exhibit a standard deviation $\sigma(\varepsilon_i) > 1$. On the contrary, if the uncertainty values are overestimated, the distribution of $\varepsilon_i(\lambda)$ would lead to $\sigma(\varepsilon_i) < 1$. Additionally, when the distribution of $\varepsilon_i(\lambda)$ is not centred at 0 and consequently exhibits a bias, a distribution mean $\mu(\varepsilon_i) < \pm 1$ would still indicate the bias is somehow represented by the uncertainty values.

Equation (18) offers the capability to verify if $L_{WN}^{OLCI-A}(\lambda)$ data products meet accuracy requirements by determining the values of $\varepsilon_i(\lambda)$ assigning an expected uncertainty to $u_{OLCI-A,i}(\lambda)/L_{WN,i}^{OLCI-A}(\lambda)$ (*e.g.*, 5% implying $u_{OLCI-A,i}(\lambda) = 0.05 \cdot L_{WN,i}^{OLCI-A}(\lambda)$). Thus Eq. (18) provides an estimate of the uncertainties actually affecting data products by determining $\varepsilon_i(\lambda)$ with the constant value of $u_{OLCI-A,i}(\lambda)/L_{WN,i}^{OLCI-A}(\lambda)$ leading to $\sigma(\varepsilon_i(\lambda)) = 1$: *i.e.*, imposing that approximately 68% of the matchups satisfy Eq. (18).

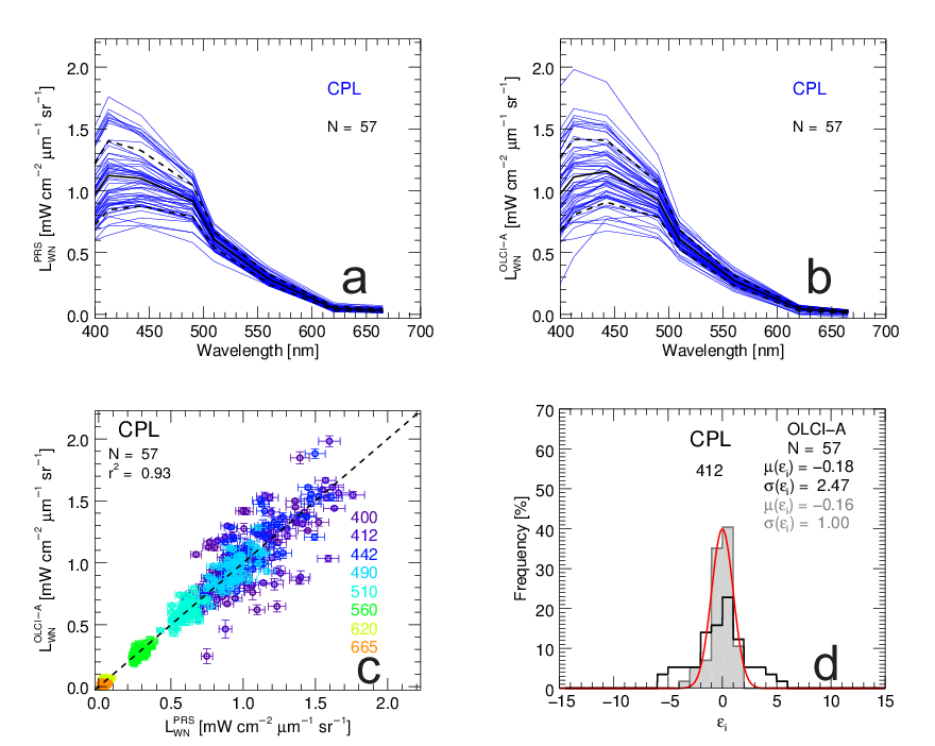

Figure 27. AERONET-OC $L_{WN}^{PRS}(\lambda)$ (a) and OLCI-A $L_{WN}^{OLCI-A}(\lambda)$ (b) matchup spectra, scatter plot of $L_{WN}^{OLCI-A}(\lambda)$ versus $L_{WN}^{PRS}(\lambda)$ matchup data (c), and distributions of the uncertainty-normalized difference ε_i at the 412 nm centre-wavelength (d) determined imposing $u_{OLCI-A,i}(412) = 0.05 \cdot L_{WN,i}^{OLCI-A}(412)$ (black line) and alternatively $\sigma(\varepsilon_i(412)) = 1$ (gray line and shaded background) compared to an ideal normal distribution (red line). The horizontal error bars in the scatter plot indicate measurement uncertainties while the vertical ones indicate the variation coefficient determined from the 3×3 image elements. N indicates the number of matchups, r^2 the determination coefficient and, $\mu(\varepsilon_i)$ and $\sigma(\varepsilon_i)$ the mean and standard deviation of the ε_i values, respectively (after Zibordi *et al.* 2022).

By omitting the dependence on λ, the mean of ε_i values, *i.e.*, $\mu(\varepsilon_i)$, and the related standard deviation, $\sigma(\varepsilon_i)$ have been computed for N pairs of satellite (*OLCI-A*) and *in situ* (*PRS*) data $[(L_{WN,1}^{OLCI-A}, L_{WN,2}^{OLCI-A}, \ldots, L_{WN,N}^{OLCI-A}), (L_{WN,1}^{PRS}, L_{WN,2}^{PRS}, \ldots, L_{WN,N}^{PRS})]$ where the subscripts 1, 2 …, N indicate the matchup index. Results from a specific case study relying on AERONET-OC data from a site characterized by oligotrophic waters, are summarized in Fig. 27 for the spectral band centred at 412 nm. These results, obtained imposing $u_{OLCI-A,i}(412) = 0.05 \cdot L_{WN,i}^{OLCI-A}(412)$ and leading to $\sigma(\varepsilon_i) > 1$ or alternatively setting $\sigma(\varepsilon_i(412)) = 1$ leading to $\mu\left(u_{SAT,i}(\varepsilon_i(\sigma(\varepsilon_i) = 1))/L_{WN,i}^{SAT}\right) > 0.05$, both indicate uncertainties for *OLCI-A* at 412 nm exceeding 5% in oligotrophic waters. Comprehensive results for key OLCI-A centre-wavelengths are provided in Table 5.

It is emphasized that the applied methodology, which attempts to overcome the limitations of common assessment schemes relying on the statistical analysis of differences between satellite and *in situ* data, allows to account for the uncertainties affecting the *in situ* data and additionally to account for the spatio-temporal perturbations characterizing the involved data. Nevertheless, despite of the ideal concept, implementations may impose the use of practical solutions. In the study proposed by Zibordi *et al.* (2022) the uncertainties for individual *in situ* measurements were determined statistically. Also, the contribution of spatio-temporal effects were quantified statistically for the *in situ* data, and solely from the 3×3 inter-pixel variability for satellite data. Still, the limitations implicit of these assumptions were minimized by restricting the time difference between satellite and *in situ* data (*i.e.*, choosing Δt = 2 hr), and also by constraining the spatial variability affecting satellite data contributing to matchups (*i.e.*, choosing a variation coefficient lower than 0.2 for the 3×3 pixels at 560 nm). Still, it is acknowledged that the above assumptions, combined with a non-normal distribution of the uncertainty-normalized differences ε_i, may all lead to a likely overestimate of actual uncertainties for $L_{WN,i}^{OLCI-A}(\lambda)$. Also, the large uncertainties characterizing the *in situ* data and the spatio-temporal variabilities, more pronounced at the red centre-wavelengths, decrease the sensitivity of the method. Finally, it is emphasized that the study by Zibordi *et al.* (2022) clearly shows that the statistical indices ψ and |ψ| commonly used to report results on matchup analysis through bias and dispersion, cannot be used as uncertainty estimates when big biases affect the data comparison or when *in situ* uncertainties or spatio-temporal variabilities are large.

Table 7 Results from the OLCI-A $L_{WN}^{OLCI-A}(\lambda)$ uncertainty analysis performed at the centre-wavelengths 400, 412, 442, 490, 560 and 665 nm. The symbols $\mu(L_{WN,i}^{PRS})$, $\mu(u_{PRS,i}/L_{WN,i}^{PRS})$, $\mu(v_{OLCI-A,i}/L_{WN,i}^{OLCI-A})$, $\mu\left(\varepsilon_i(u_{OLCI-A,i} = 0.05 \cdot L_{WN,i}^{OLCI-A})\right)$, $\mu(\varepsilon_i(\sigma(\varepsilon_i) = 1))$ indicate the mean of: the *in situ* $L_{WN,i}^{PRS}$, the related relative uncertainties, the relative variance of satellite $L_{WN,i}^{OLCI-A}(\lambda)$, the ε_i computed setting $u_{SAT,i}(\lambda) = 0.05 \cdot L_{WN,i}^{OLCI-A}(\lambda)$ and the ε_i determined imposing $\sigma(\varepsilon_i(\lambda)) = 1$. The ± values indicate the standard deviations. The quantities $|\psi|$ and ψ are the mean of absolute relative differences and the mean of relative differences between $L_{WN,i}^{PRS}(\lambda)$ and $L_{WN,i}^{OLCI-A}(\lambda)$. Finally, $\mu(u_{OLCI-A,i}(\varepsilon_i(\sigma(\varepsilon_i) = 1))/L_{WN,i}^{OLCI-A})$ indicates the mean of the estimated satellite uncertainties quantified imposing $\sigma(\varepsilon_i) = 1$ (reprinted from Zibordi *et al*. 2022).

λ [nm]	400	412	442	490	560	665
$\mu(L_{WN,i}^{PRS}) \pm \sigma(L_{WN,i}^{PRS})$ [mW cm^{-2} µm^{-1} sr^{-1}]	0.972±0.248	1.123±0.279	1.100±0.224	0.916±0.128	0.285±0.038	0.030±0.014
$\mu(u_{PRS,i}/L_{WN,i}^{PRS}) \pm \sigma(u_{PRS,i}/L_{WN,i}^{PRS})$	0.050±0.002	0.049±0.002	0.049±0.002	0.051±0.002	0.073±0.004	0.404±0.163
$\mu(v_{SAT,i}/L_{WN,i}^{SAT}) \pm \sigma(v_{SAT,i}/L_{WN,i}^{SAT})$	0.035±0.036	0.031±0.024	0.025±0.016	0.020±0.012	0.039±0.021	0.469±0.988
$\|\psi\|$	0.144	0.130	0.088	0.070	0.104	0.434
ψ	–0.002	–0.007	+0.026	+0.005	–0.037	–0.227
$\mu\left(\varepsilon_i(u_{SAT,i} = 0.05 \cdot L_{WN,i}^{SAT})\right) \pm \sigma(\varepsilon_i)$	–0.06±2.90	–0.18±2.47	+0.66±1.67	+0.12±1.31	–0.41±1.32	–0.88±1.47
$\mu(\varepsilon_i(\sigma(\varepsilon_i) = 1)) \pm \sigma(\varepsilon_i(\sigma(\varepsilon_i) = 1))$	–0.15±1.00	–0.16±1.00	+0.36±1.00	+0.07±1.00	–0.35±1.00	–0.66±1.00
$\mu(u_{SAT,i}(\varepsilon_i(\sigma(\varepsilon_i) = 1))/L_{WN,i}^{SAT})$	0.302	0.203	0.107	0.080	0.100	0.920

19 Summary

This document reviews the basic elements underpinning above-water radiometry and aims at providing guidance to scientists approaching *in situ* measurements for ocean colour applications with focus on the assessment of satellite data products. The document, that benefits for extracts from various publications, provides recommendations complementing community protocols with a pragmatic view to field equipment, instruments calibration and characterization, measurement practices, quality assurance, data reduction and processing, quality control, quantification of uncertainties, and application of data to the assessment of satellite data products.

20 References

Białek A., Douglas S., Kuusk J., Ansko I., Vabson V., Vendt R. and Casal T., 2020: Example of Monte Carlo method uncertainty evaluation for above-water ocean colour radiometry. *Remote Sensing*, 12 (5), 780, doi:10.3390/rs12050780.

Bulgarelli B. and Zibordi G., 2018: On the detectability of adjacency effects in ocean colour remote sensing of mid-latitude coastal environments by SeaWiFS, MODIS-A, MERIS, OLCI, OLI and MSI. *Remote Sensing of Environment*, 209, 423–438.

Bulgarelli B. and Zibordi G., 2020: Adjacency radiance around a small island: Implications for system vicarious calibrations. *Applied Optics*, 59 (10), 63-69.

Carder K. L. and Steward R. G., 1985: A remote-sensing reflectance model of a red-tide dinoflagellate off west Florida 1. *Limnology and oceanography*, 30 (2), 286–298.

Carrizo C, Gilerson A., Foster R., Golovin A. and El-Habashi A., 2019: Characterization of radiance from the ocean surface by hyperspectral imaging. *Optics Express*, 27 (2), 1750–1768.

Cazzaniga I. and Zibordi G., 2023: AERONET-OC L_{WN} Uncertainties: Revisited. *Journal of Atmospheric and Oceanic Technology*, 40 (4), 411–425.

Concha J. A., Bracaglia M. and Brando, V. E., 2021: Assessing the influence of different validation protocols on Ocean Colour match-up analyses. *Remote Sensing of Environment*, *259*, 112415.

Cox C. and Munk, W., 1954: Measurement of the roughness of the sea surface from photographs of the sun's glitter. *Journal of the Optical Society of America* 44, 11838–11850.

Foster R. and Gilerson A., 2016: Polarized transfer functions of the ocean surface for above-surface determination of the vector submarine light field. *Applied Optics*, 55 (33), 9476–9494.

Fougnie B., Frouin R., Lecomte P. and Deschamps P.-Y., 1999: Reduction of skylight reflection effects in the above-water measurement of diffuse marine reflectance. *Applied Opt*ics 38, 3844–3856.

D'Alimonte D. and Kajiyama T., 2016: Effects of light polarization and waves slope statistics on the reflectance factor of the sea surface. *Optics Express*, 24 (8), 7922–7942.

D'Alimonte D., Kajiyama T., Zibordi G. and Bulgarelli B., 2021: Sea-surface reflectance factor: replicability of computed values. *Optics Express*, 29(16), 25217-25241.

EUMETSAT, 2018: Sentinel-3 OLCI Marine User Handbook, EUM/OPS-SEN3/MAN/17/907205, https://www.eumetsat.int/media/45743.

Gergely M. and Zibordi, G. 2014: Assessment of AERONET-OC Lwn uncertainties. *Metrologia*, 51(1), 40-47.

Gleason A. C. *et al*., 2012: Detailed validation of the bidirectional effect in various Case I and Case II waters. *Optics Express*, 20 (7), 7630–7645.

Gordon H. R. and Clark D. K., 1981: Clear water radiances for atmospheric correction of coastal zone colour scanner imagery. *Applied Optics*, 20 (24), 4175–4180.

Grégis F., 2019: On the meaning of measurement uncertainty. Measurement - Journal of the International Measurement Confederation (IMEKO), 41–46, 10.1016/j.measurement.2018.09.073.ffhalshs-01884155.

Groetsch P.M., Gege P., Simis S.G., Eleveld M.A. and Peters S.W., 2017: Validation of a spectral correction procedure for sun and sky reflections in above-water reflectance measurements. *Optics Express*, 25 (16), A742-A761.

JCGM, 2008: Evaluation of measurement data – Guide to the expression of uncertainty in measurement. *Int. Organ. Stand Geneva ISBN*, 50, 134 pp.

Harmel T., 2023: Apparent surface-to-sky radiance ratio of natural waters including polarization and aerosol effects: implications for above-water radiometry. *Frontiers in Remote Sensing*, 4, 1307976.

Hooker S.B. and Morel A., 2003: Platform and environmental effects on above-water determinations of water-leaving radiances. *Journal of Atmospheric and Oceanic Technology*, 20 (1), 187–205.

Hooker S.B., Lazin G., Zibordi G. and McLean S., 2002: An evaluation of above-and in-water methods for determining water-leaving radiances. *Journal of Atmospheric and Oceanic Technology*, 19 (4), 486–515.

Hooker S.B. and Zibordi G., 2005: Platform perturbations in above-water radiometry. *Applied Optics*, 44 (4), 553–567.

Hooker S.B., Zibordi G., Berthon J.F. and Brown J.W., 2004: Above-water radiometry in shallow coastal waters. *Applied Optics*, 43 (21), 4254–4268.

Hooker, S.B., G. Zibordi, J-F. Berthon, D. D'Alimonte, S. Maritorena, S. McLean, and J. Sildam, 2001: Results of the Second SeaWiFS Data Analysis Round Robin, March 2000 (DARR-00). *NASA Tech. Memo. 2001–206892, Vol. 15,* S.B. Hooker and E.R. Firestone, Eds., NASA Goddard Space Flight Center, Greenbelt, Maryland, 71 pp.

Hooker S.B., G. Zibordi, J-F. Berthon, D. D'Alimonte, D. van der Linde and J.W. Brown, 2003: Tower-Perturbation Measurements in Above-Water Radiometry. *NASA Tech. Memo. 2003–206892, Vol. 23,* S.B. Hooker and E.R. Firestone, Eds., NASA Goddard Space Flight Center, Greenbelt, Maryland, 35 pp.

Hunt S. E. *et al.*, 2020: Comparison of the Sentinel-3A and B SLSTR tandem phase data using metrological principles. *Remote Sensing*, 12 (18), 1–23.

Immler F. J., Dykema J., Gardiner T., Whiteman D. N. and Thorne P. W., 2010: Reference Quality Upper-Air Measurements : guidance for developing GRUAN data products. *Atmospheric Measurement Technology*, 3 (5), 1217–1231.

Kutser T., Vahtmäe E., Paavel B. and Kauer T., 2013: Removing glint effects from field radiometry data measured in optically complex coastal and inland waters. *Remote Sensing of Environment*, 133, 85–89.

Lee Z.P., Du K., Voss K.J., Zibordi G., Lubac B., Arnone R. and Weidemann A., 2011: An inherent-optical-property-centered approach to correct the angular effects in water-leaving radiance. *Applied Optics*, 50 (19), 3155–3167.

Lee Z., Carder K. L., Steward R. G., Peacock T. G., Davis C. O. and Mueller J. L., 1997: Remote sensing reflectance and inherent optical properties of oceanic waters derived from above-water measurements. In *Ocean Optics XIII*, SPIEE Vol. 2963, 160–166.

Mekaoui S. and Zibordi G., 2013: Cosine error for a class of hyperspectral irradiance sensors. *Metrologia*, 50 (3), 187.

Mobley C.D., 1999: Estimation of the remote-sensing reflectance from above-surface measurements. *Applied Optics* 38, 7442–7455.

Mobley C.D., 2015: Polarized reflectance and transmittance properties of windblown sea surfaces. *Applied Optics* 54 (15), 4828–4849.

Morel A., Antoine D. and Gentili B., 2002: Bidirectional reflectance of oceanic waters: accounting for Raman emission and varying particle scattering phase function. *Applied Optics*, 41 (30), 6289–6306.

Mueller J. L., and Austin R. W., 1995: Ocean Optics Protocols for SeaWiFS Validation, Revision 1. *NASA Tech. Memo. 104566, Vol.* ***25****,* S.B. Hooker, E.R. Firestone and J.G. Acker, Eds., NASA Goddard Space Flight Center, Greenbelt, Maryland, 67 pp.

Palmer J. M. and Grant B. G., 2010: The Art of Radiometry. Vol. PM184. Bellingham, WA: SPIE.

Pitarch, J., Talone, M., Zibordi, G., and Groetsch, P., 2020: Determination of the remote-sensing reflectance from above-water measurements with the "3C model": a further assessment. *Opt Express,* **28**(11), 15885–15906.

Ruddick K.G., De Cauwer V., Park Y. J. and Moore G., 2006: Seaborne measurements of near infrared water-leaving reflectance: The similarity spectrum for turbid waters. *Limnology and Oceanography,* 51 (2), 1167–1179.

Simis S. G. and Olsson J., 2013: Unattended processing of shipborne hyperspectral reflectance measurements. *Remote Sensing of Environment*, 135, 202-212.

Talone M., and Zibordi G., 2018: Non-linear response of a class of hyper-spectral radiometers. *Metrologia*, *55* (5), 747.

Talone M. and Zibordi G. 2019: Spectral assessment of deployment platform perturbations in above-water radiometry. *Optics Express,* 27 (12), A878–A889.

Talone M., Zibordi G. and Lee Z., 2018: Correction for the non-nadir viewing geometry of AERONET-OC above water radiometry data: An estimate of uncertainties. *Optics Express*, 26 (10), A541−A561.

Talone M., Zibordi G., Ansko I., Banks A. C. and Kuusk J., 2016: Stray light effects in above-water remote-sensing reflectance from hyperspectral radiometers. *Applied Optics*, 55 (15), 3966−3977.

Talone M., Zibordi G. and Lee Z., 2018: Correction for the non-nadir viewing geometry of AERONET-OC above water radiometry data: an estimate of uncertainties. *Optics Express,* 26 (10), A541–A561.

Talone M., Zibordi G., and Pitarch J., 2024: On the application of AERONET-OC multispectral data to assess satellite derived hyperspectral R_{rs}. *IEEE Geoscience and Remote Sensing Letters*, doi: 10.1109/LGRS.2024.3350928.

Thuillier G. *et al.*,: 2003: The solar spectral irradiance from 200 to 2400 nm as measured by the SOLSPEC spectrometer from the ATLAS and EURECA missions. *Solar Physics*, 214, 1–22.

Vabson V., Ansko I., Vendt R. and Kuusk J., 2023: *Guidelines for individual OCR full characterisation and calibration. Technical Report* FRM4SOC2-D8, EUMETSAT Contract n. EUM/CO/21/460002539/JIG Fiducial Reference Measurements for Satellite Ocean Colour (FRM4SOC Phase-2), pp. 31.

Vardeman S.B. and Jobe J.M., 2016: *Statistical methods for quality assurance*. Springer-Verlag New York.

Wunsch C., Schmitt R. W. and Baker D. J., 2013: Climate change as an intergenerational problem, *Proceedings of the National Academy of Sciences*, 110, 4435–4436.

Zemek F. (2014): *Airborne remote sensing: theory and practice in assessment of terrestrial ecosystems*. Global Change Research Centre AS CR, pp. 159.

Zhang X., He S., Shabani A., Zhai P.W. and Du K., 2017: Spectral sea surface reflectance of skylight. *Optics Express*, 25 (4), A1–A13.

Zibordi G., 2012: Comment on "Long Island Sound Coastal Observatory: assessment of above-water radiometric measurement uncertainties using collocated multi and hyperspectral systems". *Applied Optics*, 51 (17), 3888–3892.

Zibordi G., 2016: Experimental evaluation of theoretical sea surface reflectance factors relevant to above-water radiometry. *Optics Express*, 24 (6), A446–A459.

Zibordi G. and Berthon J-F., 2024: Coastal Atmosphere & Sea Time Series (CoASTS) and Bio-Optical mapping of Marine optical Properties (BiOMaP): the CoASTS-BiOMaP dataset. *Earth System Science Data* (submitted).

Zibordi G., Berthon J-F., Doyle J.P., Grossi S., van der Linde D., Targa C. and Alberotanza L., 2002: Coastal Atmosphere and Sea Time Series (CoASTS), Part 1: A Tower-Based Long-Term Measurement Program. *NASA Tech. Memo. 2002–206892, Vol. 19,* S.B. Hooker and E.R. Firestone, Eds., NASA Goddard Space Flight Center, Greenbelt, Maryland, 29 pp.

Zibordi G. and Bulgarelli B., 2007: Effects of cosine error in irradiance measurements from field ocean colour radiometers. *Applied Optics*, 46 (22), 5529–5538.

Zibordi G., D'Alimonte D. and Kajiyama T. 2022: Automated Quality Control of AERONET-OC L WN Data. *Journal of Atmospheric and Oceanic Technology*, 39 (12), 1961–1972.

Zibordi G., D'Alimonte D., Bulgarelli B., Kajiyama T. and Slutsker I., 2025: On the impact of alternative processing on AERONET-OC L_{WN}. *Atmospheric and Oceanic Technology*, under revision.

Zibordi G., Holben B. N., Talone M., D'Alimonte D., Slutsker I., Giles D. M. and Sorokin M. G. 2021: Advances in the ocean colour component of the aerosol robotic network (AERONET-OC). *Journal of Atmospheric and Oceanic Technology*, 38 (4), 725–746.

Zibordi G., Hooker S.B., Berthon J.F. and D'Alimonte D., 2002: Autonomous above-water radiance measurements from an offshore platform: a field assessment experiment. *Journal of Atmospheric and Oceanic Technology*, 19 (5), 808–819.

Zibordi G., Kwiatkowska E., Mélin F., Talone M., Cazzaniga I., Dessailly D. and Gossn J. I. 2022: Assessment of OLCI-A and OLCI-B radiometric data products across European seas. *Remote Sensing of Environment*, *272*, https://doi.org/10.1016/j.rse.2022.112911.

Zibordi G., Mélin F., Bulgarelli B., Canuti E. and Berthon J.-F., 2020: Ocean Colour Calibration and Validation: The JRC Contribution to Copernicus. EUR 30408 EN, Publications Office of the European Union, Luxembourg, ISBN 978-92-76-23474-6, doi:10.2760/984004, JRC122212.

Zibordi G., Mélin F. and Berthon J.-F., 2006: Comparison of SeaWiFS, MODIS and MERIS radiometric products at a coastal site. *Geophysical Research Letters*, 33 (6), L06617, doi:10.1029/2006GL025778.

Zibordi G., Mélin F., Berthon J.-F., Holben B., Slutsker I., Giles D., D'Alimonte D., Vandemark D., Feng H., Schuster G. and Fabbri B.E., 2009: AERONET-OC: a network for the validation of ocean colour primary products. *Journal of Atmospheric and Oceanic Technology*, 26 (8), 1634–1651.

Zibordi G., Ruddick K., Ansko I., Moore G., Kratzer S., Icely J. and Reinart A., 2012: In situ determination of the remote sensing reflectance: an inter-comparison. *Ocean Science*, 8 (4), 567–586.

Zibordi G., Talone M., 2025: Operational correction for the temperature dependence of a class of hyperspectral radiometers. *Journal of Atmospheric and Oceanic Technology*, under revision.

Zibordi G., Talone M. and Mélin, F. 2022: Uncertainty estimate of satellite-derived normalized water-leaving radiance. *IEEE Geoscience and Remote Sensing Letters*, 19, 1–5.

Zibordi G., Talone M. and Jankowski L. 2017: Response to temperature of a class of in situ hyperspectral radiometers. *Journal of Atmospheric and Oceanic Technology*, 34 (8), 1795–1805.